Journal of Computational Physics 463 (2022) 111292

Contents lists available at ScienceDirect

Journal of Computational Physics

www.elsevier.com/locate/jcp

A hybrid WENO scheme for steady-state simulations of Euler equations

Yifei Wan, Yinhua Xia *,[1]

School of Mathematical Sciences, University of Science and Technology of China, Hefei, Anhui 230026, PR China

ARTICLE INFO

Article history:
Received 7 December 2021
Received in revised form 27 March 2022
Accepted 8 May 2022
Available online 16 May 2022

Keywords:
Euler equations
Steady-state convergence
Hybrid scheme
WENO reconstruction
Finite difference method

ABSTRACT

For strong shock waves in solutions of steady-state Euler equations, the high-order shock capturing schemes usually suffer from the difficulty of convergence of residue close to machine zero. Several new weighted essentially non-oscillatory (WENO) type schemes have recently been designed to overcome this long-standing issue. In this paper, a new hybrid strategy is proposed for the fifth-order WENO scheme to simulate steady-state solutions of Euler equations. Compared with the existing WENO schemes, the hybrid WENO scheme performs better steady-state convergence property with less dissipative and dispersive errors. Meanwhile, the essentially oscillation-free feature is kept. In the hybrid strategy, the stencil is distinguished into smooth, non-smooth, or transition regions, which is realized by a simple smoothness detector based on the smoothness indicators in the original WENO method. The linear reconstruction and the specific WENO reconstruction are applied to the smooth and non-smooth regions, respectively. In the transition region, the mixture of the linear and WENO reconstructions is adopted by a smooth transitive interpolation, which plays a vital role in the steady-state convergence for the hybrid scheme. Numerical comparisons and spectral analysis are presented to demonstrate the robust performance of the new hybrid scheme for steady-state Euler equations.

1. Introduction

The steady-state solutions to Euler equations

$$\boldsymbol{F}(\boldsymbol{U})_x + \boldsymbol{G}(\boldsymbol{U})_y + \boldsymbol{H}(\boldsymbol{U})_z = \boldsymbol{0}, \tag{1.1}$$

take a great part in computational fluid dynamics. In (1.1), $\boldsymbol{U} = (\rho, \rho u, \rho v, \rho w, E)^T$ contains the conservative variables, $\boldsymbol{F}(\boldsymbol{U}) = (\rho u, \rho u^2 + P, \rho uv, \rho uw, u(E+P))^T$, $\boldsymbol{G}(\boldsymbol{U}) = (\rho v, \rho uv, \rho v^2 + P, \rho vw, v(E+P))^T$ and $\boldsymbol{H}(\boldsymbol{U}) = (\rho w, \rho uw, \rho vw, \rho w^2 + P, w(E+P))^T$ are the fluxes in x, y and z directions, respectively. Here u, v and w are the velocities in the x, y and z directions, and ρ is the density. $E = \frac{P}{\gamma-1} + \frac{1}{2}\rho(u^2+v^2+w^2)$ is the total energy, P is the pressure, and γ is the radio of specific heats.

In order to solve equations (1.1), one choice is to get the steady-state solutions of unsteady Euler equations with an appropriate time marching method. If the residue (some approximation to the time derivative) is small enough, the steady-

* Corresponding author.
E-mail addresses: wanyifei@mail.ustc.edu.cn (Y. Wan), yhxia@ustc.edu.cn (Y. Xia).

[1] Research supported by the NSFC grant No. 11871449.

https://doi.org/10.1016/j.jcp.2022.111292

state solutions of (1.1) are obtained. However, the existence of strong discontinuities brings great difficulty in numerical simulations, since some oscillations may appear and prevent the residue from converging to the ideal level, close to machine zero. Thus, we need a robust scheme to solve (1.1) and keep the high-resolution property simultaneously. By identifying the smoothest stencil for reconstruction, Harten et al. [23] proposed the essentially non-oscillatory (ENO) scheme to solve one-dimensional unsteady problems. Afterward, Liu et al. [38] designed the original weighted essentially non-oscillatory (WENO) scheme based on the convex combination of the sub-stencils. Since the weight of the stencil containing shock is compressed nearly zero, the essentially non-oscillatory property is achieved. To improve the accuracy, Jiang and Shu [28] designed a new smoothness indicator that was widely used in lots of WENO schemes. This WENO scheme could obtain the optimal accuracy in a smooth region, which is termed the WENO-JS scheme in this paper. Nevertheless, the WENO-JS scheme may lose some resolution near critical points. To overcome this defect, Henrick et al. [24] proposed a mapping WENO scheme by modifying the nonlinear weight. However, this strategy increased about 20% CPU time. Later, Borges et al. [4] pointed out that the numerical solution given by the WENO-M scheme only recovers resolution satisfactorily near first-order critical points, and developed the WENO-Z scheme, which can successfully handle higher-order critical points by tuning the parameter. Meanwhile, it had been pointed out by Acker et al. in [1] that increasing the weight of the non-smooth stencil is of great importance to give better resolution on the coarse grid, while increasing the accuracy near critical points works on the fine grid. Thus, many papers focused on these points to devise new WENO schemes [1,12,17,19,27,32,37,39,45,57,58] to improve the accuracy and efficiency.

Another popular strategy in the development of WENO schemes is the hybrid approach to improve the performance, such as conservative hybrid compact-WENO schemes [42], hybrid compact-ENO scheme [2], hybrid Hermite WENO scheme [62], multi-domain hybrid spectral-WENO methods [10], characteristic-wise hybrid compact-WENO scheme [46], high-spectral resolution hybrid finite-difference method [16], hybrid compact-WENO finite difference schemes with shock detectors based on the radial basis function [53], conjugate Fourier algorithm [13], and artificial neural network [54], etc. The performances of these hybrid methods are heavily dependent on the proposed shock detectors. Thus, the design of shock detectors has become a hot topic for WENO schemes nowadays. There appeared a great deal of shock detectors, such as the minmod-based TVB limiter [9], discontinuity indicator based on the average total variation of the solution [44,64], a shock-detection technique by Krivodonova et al. [29], Harten's multi-resolution analysis [22], shock detection method based on radial basis function [53], the trigonometric detector-based conjugate Fourier analysis [13], monotonicity-preserving discontinuity indicator [51], the shock detection method based on neural network [50,54], and shock detection method based on targeted ENO schemes [17,18], etc.

The classic WENO and hybrid WENO schemes made a great success in the simulations of unsteady problems; however, when they are adopted to solve steady-state problems with strong shock waves, the residue of numerical solution usually hangs at the level of truncation error even after long time iterations. Serna and Marquina [47] reconstructed the numerical flux by a new kind of limiter, and experiments verified the improvement of the convergence to the steady-state. Zhang and Shu [60,61] pointed out that the appearance of slight post-shock oscillations has a significant impact on steady-state convergence, which leads to the residue hanging at a relatively high level rather than settling down to machine zero. Afterward, the numerical results in [59,61] indicated that the upwind-biased interpolation technique is helpful for steady-state convergence. However, it still seems difficult for the residue to converge to machine zero when the shock passes through the boundary. Chen et al. [7] used fast sweeping methods with Lax-Friedrichs numerical fluxes to solve steady-state hyperbolic conservation laws and developed novel multigrid fast sweeping methods [8] to improve steady-state convergence. Engquist et al. [14,15] showed that fast sweeping methods could solve conservation laws at the steady-state with high resolution and low computational cost. Hao et al. [21] suggested abandoning time marching and using the homotopy method to solve the nonlinear system obtained by WENO discretizations. The drawback is that one should solve the nonlinear system carefully because of the non-uniqueness of solutions. Hu et al. [25,26] solved steady Euler equations with non-oscillatory k-exact reconstruction and enhanced the numerical accuracy of problems containing curved boundaries by non-uniform rational B-splines [40]. Chen [6] and Wu et al. [56,61] proposed a new fixed-point sweeping WENO method to solve hyperbolic conservation law. However, the convergence failure to the steady state still existed, although the convergence property was improved significantly. Zhu et al. [61,65–69] proposed new schemes based on the central WENO (CWENO) and multi-resolution WENO (MRWENO) reconstructions to solve unsteady and steady problems. These schemes showed the lovely convergence property for the steady-state solutions, including extensive benchmark examples. However, some oscillations may appear near discontinuities because the schemes perform similarly to a linear scheme here. In [36], Li et al. combined the fixed-point fast sweeping method with multi-resolution WENO reconstruction to solve steady problems and utilized the immersed boundary method [41] to deal with curved boundaries. In [70], Zhu et al. developed multi-resolution WENO limiters to solve steady-state problems with Runge-Kutta discontinuous Galerkin methods; besides, the new multi-resolution WENO limiters are easy to be constructed and extended to the higher order.

Meanwhile, few hybrid schemes are applied to steady-state simulations since the gap between different kinds of approximations hinders the convergence of residue. Recently, a new hybrid strategy [52] has been proposed to Euler equations with the fifth-order WENO finite difference schemes. The fifth-order WENO scheme is the most popular one among all the high order WENO schemes because some oscillations may appear for higher order WENO schemes due to the usage of larger sub-stencil; meanwhile, this scheme maintains sufficiently low dissipation to capture strong discontinuities. Spectral analysis and numerical results of unsteady problems demonstrated that the hybrid schemes maintain less dispersion and dissipation errors than the original schemes, and resolve more flow field details, especially in the multi-scale region. Following this work, we apply this new hybrid approach to steady-state simulations.

In this paper, we design a new hybrid finite difference scheme to simulate steady-state solutions, which can give numerical solutions with lower dissipation than the central WENO and multi-resolution WENO schemes, and the essentially non-oscillatory property can be achieved. For general hybrid methods [33–35,62,63], people always classify the whole domain into two parts: the smooth region and the non-smooth region, and the corresponding linear reconstruction is used in the smooth region while specific WENO reconstruction in the non-smooth region. Different from the general approach, we classify the whole region into three parts: smooth, non-smooth, and transition regions. An elementary shock detector is adopted to distinguish these regions from the entire domain, which is based on the smoothness indicator in the WENO-JS [28] reconstruction and similar to the approach in [3] for the third-order WENO scheme. This shock detector could effectively identify the smooth region and critical points and keep the optimal accuracy in the smooth region while extra nonphysical oscillation is avoided. The linear reconstruction is used in the smooth region. Besides, a blending reconstruction is developed in the non-smooth region based on the smoothness amplification factor, which can significantly decrease dissipative and dispersive errors. In the transition region, a smooth transitive reconstruction of the smooth region and the non-smooth region is adopted, which also plays an important role in steady-state convergence for the hybrid scheme. Aiming to weaken the WENO reconstruction's linearity, a new kind of nonlinear weight is proposed in this hybrid scheme. Therefore, compared with the numerical performances of the central WENO and multi-resolution WENO schemes, the new hybrid one could maintain a good balance between the steady-state convergence and compressing oscillations near discontinuities.

The rest of the paper is organized as follows. Section 2 will briefly review the WENO finite difference method for hyperbolic conservation laws, including the central WENO and multi-resolution reconstructions. Section 3 is devoted to the description of the new hybrid strategy. In the beginning, we propose a simple detector to distinguish three different regions, which is based on the smoothness indicator in the classical WENO-JS [28] reconstruction. After that, a blending reconstruction in the non-smooth region is developed. Then, we present a smoothing interpolation technique in the transition region to complete the whole hybrid scheme. Finally, the approximate spectral analysis is applied to show the good performance of the hybrid scheme on the dispersion and dissipation relations. In Section 4, numerous experiment results for benchmark problems show the excellent steady-state convergence and essentially non-oscillation properties of the new hybrid WENO scheme compared with the central WENO and multi-resolution WENO schemes. Conclusions and perspectives are drawn in Section 5.

2. The WENO finite difference method

This section will briefly review the finite difference method with the sliding operator and the WENO reconstruction.

2.1. The conservative finite difference method

We consider the one-dimensional scalar equation

$$f(u)_x = 0,\ x \in [a, b]. \tag{2.1}$$

Consider a uniform grid, $a = x_{\frac{1}{2}} < x_{\frac{3}{2}} < \cdots < x_{N+\frac{1}{2}} = b$. Let $I_i = [x_{i-\frac{1}{2}}, x_{i+\frac{1}{2}}]$, $\Delta x = x_{i+\frac{1}{2}} - x_{i-\frac{1}{2}}$ and x_i is the center of the cell I_i for $i = 1, 2, \cdots, N$. Let $h(x)$ be the sliding function satisfying

$$\frac{\int_{x-\frac{\Delta x}{2}}^{x+\frac{\Delta x}{2}} h(\xi)d\xi}{\Delta x} = f(u(x,t)), \tag{2.2}$$

then

$$f(u)_x = \frac{h(x+\frac{\Delta x}{2}) - h(x-\frac{\Delta x}{2})}{\Delta x}. \tag{2.3}$$

Thus, the spatial derivative operator can be discretized as

$$L(u_i) = \frac{\hat{f}_{i+\frac{1}{2}} - \hat{f}_{i-\frac{1}{2}}}{\Delta x}, \tag{2.4}$$

where u_i is the numerical approximation to the point value $u(x_i, t)$ and the numerical flux $\hat{f}_{i+\frac{1}{2}}$ is the approximation of $h(x_{i+\frac{1}{2}}, t)$ obtained by reconstruction. In the reconstruction, $f(u_i)$ can be regarded as the approximation of the cell average of the sliding function $\bar{h}_i = \frac{1}{\Delta x}\int_{x_{i-\frac{1}{2}}}^{x_{i+\frac{1}{2}}} h(x)dx$. Therefore, we can reconstruct $\hat{f}_{i+\frac{1}{2}} = h_{i+\frac{1}{2}}$ from the cell average $\bar{h}_i$. For sake of maintaining stability, the upwind mechanism is performed by the flux splitting, e.g. the Lax-Friedrichs splitting $\hat{f}_{i+\frac{1}{2}} = \hat{f}^+_{i+\frac{1}{2}} + \hat{f}^-_{i+\frac{1}{2}}$ with $f^{\pm}(u) = \frac{1}{2}(f(u) \pm \alpha u)$ and $\alpha = \max_u |f'(u)|$ chosen in the relevant region.

Similarly, for the one-dimensional system

$$\boldsymbol{f}(\boldsymbol{u})_x = \boldsymbol{0}, x \in [a, b], \tag{2.5}$$

the spatial derivative operator can be discretized as

$$L(\boldsymbol{u}_i) = \frac{\hat{\boldsymbol{f}}_{i+\frac{1}{2}} - \hat{\boldsymbol{f}}_{i-\frac{1}{2}}}{\Delta x}, \tag{2.6}$$

where $\boldsymbol{u}_i$ is the approximation to $\boldsymbol{u}(x_i, t)$. As a natural choice, we can reconstruct $\hat{\boldsymbol{f}}_{i+\frac{1}{2}}$ in a component-wise fashion. However, for more demanding problems or when the resolution of approximation is high, the more robust characteristic decomposition is needed. Let $\boldsymbol{R} = \boldsymbol{R}(\boldsymbol{u}_{i+\frac{1}{2}}), \boldsymbol{L} = \boldsymbol{R}^{-1}(\boldsymbol{u}_{i+\frac{1}{2}}), \boldsymbol{\Lambda} = \boldsymbol{\Lambda}(\boldsymbol{u}_{i+\frac{1}{2}})$ be the matrices of right eigenvectors, left eigenvectors, and eigenvalues of the Jacobian $\boldsymbol{f}'(\boldsymbol{u}_{i+\frac{1}{2}})$ respectively. The average state $\boldsymbol{u}_{i+\frac{1}{2}}$ can be computed by a Roe average satisfying

$$\boldsymbol{f}(\boldsymbol{u}_{i+1}) - \boldsymbol{f}(\boldsymbol{u}_i) = \boldsymbol{f}'(\boldsymbol{u}_{i+\frac{1}{2}})(\boldsymbol{u}_{i+1} - \boldsymbol{u}_i). \tag{2.7}$$

Transform the point value $\boldsymbol{u}_j$ and $\boldsymbol{f}(\boldsymbol{u}_j)$ into local characteristic field by

$$\boldsymbol{v}_j = \boldsymbol{L}\boldsymbol{u}_j, \boldsymbol{g}_j = \boldsymbol{L}\boldsymbol{f}_j, j = i-2, \cdots, i+3. \tag{2.8}$$

Next, we adopt the Lax-Friedrichs flux splitting for each characteristic variable and the WENO reconstruction to obtain the corresponding component of the flux $\hat{\boldsymbol{g}}^{\pm}_{i+\frac{1}{2}}$. In the Lax-Friedrichs flux splitting, the maximum characteristic speed can be set as $\alpha = \max_j |\lambda_l(\boldsymbol{u}_j)|$ for each characteristic variable in the relevant region. Then we project the new flux $\hat{\boldsymbol{g}}^{\pm}_{i+\frac{1}{2}}$ back into physical space by

$$\hat{\boldsymbol{f}}^{\pm}_{i+\frac{1}{2}} = \boldsymbol{R}\hat{\boldsymbol{g}}^{\pm}_{i+\frac{1}{2}}. \tag{2.9}$$

The final numerical flux is given by $\hat{\boldsymbol{f}}_{i+\frac{1}{2}} = \hat{\boldsymbol{f}}^{+}_{i+\frac{1}{2}} + \hat{\boldsymbol{f}}^{-}_{i+\frac{1}{2}}$.

For a multi-dimensional system, a similar procedure can be performed in a dimension by dimension way to derive the corresponding finite difference scheme in conservative form. One can refer to [48,49] for more details.

Next, we describe the WENO reconstruction procedure to obtain $h_{i+\frac{1}{2}}$ from the cell average $\bar{h}_i$ of the sliding function. Generally, let $\{\bar{v}_i\}$ be the cell average of a function $v(x)$ on the uniform grid above.

2.2. The WENO-JS reconstruction

First, we describe the classical reconstruction method given in [28] that is used to solve unsteady problems. This reconstruction procedure is termed as the WENO-JS scheme in the following text. For each of the following equal-sized stencils,

$$S_1^{(1)} = \{I_{i-2}, I_{i-1}, I_i\}, S_2^{(1)} = \{I_{i-1}, I_i, I_{i+1}\}, S_3^{(1)} = \{I_i, I_{i+1}, I_{i+2}\}, \tag{2.10}$$

there is a quadratic polynomial satisfying

$$\frac{1}{\Delta x}\int_{I_j} p_3^L(\xi)d\xi = \bar{v}_j, I_j \in S_1^{(1)}, \tag{2.11}$$

$$\frac{1}{\Delta x}\int_{I_j} p_3^C(\xi)d\xi = \bar{v}_j, I_j \in S_2^{(1)}, \tag{2.12}$$

$$\frac{1}{\Delta x}\int_{I_j} p_3^R(\xi)d\xi = \bar{v}_j, I_j \in S_3^{(1)}, \tag{2.13}$$

respectively. Let $\beta_1^{(1)}, \beta_2^{(1)}, \beta_3^{(1)}$ be the smoothness indicators of $p_3^L(x), p_3^C(x), p_3^R(x)$ respectively. The smoothness indicator is computed by

$$\beta = \sum_{r=1}^{n} \Delta x^{2r-1} \int_{x_{i-\frac{1}{2}}}^{x_{i+\frac{1}{2}}} (p^{(r)}(\xi))^2 d\xi, \tag{2.14}$$

where the superscript (r) represents the order of derivative and n represents the degree of $p(x)$. The explicit formulas for $\beta_k^{(1)}$ are

$$\beta_1^{(1)} = \frac{13}{12}(\bar{v}_{i-2} - 2\bar{v}_{i-1} + \bar{v}_i)^2 + \frac{1}{4}(\bar{v}_{i-2} - 4\bar{v}_{i-1} + 3\bar{v}_i)^2, \tag{2.15}$$

$$\beta_2^{(1)} = \frac{13}{12}(\bar{v}_{i-1} - 2\bar{v}_i + \bar{v}_{i+1})^2 + \frac{1}{4}(\bar{v}_{i-1} - \bar{v}_{i+1})^2, \tag{2.16}$$

$$\beta_3^{(1)} = \frac{13}{12}(\bar{v}_i - 2\bar{v}_{i+1} + \bar{v}_{i+2})^2 + \frac{1}{4}(3\bar{v}_i - 4\bar{v}_{i+1} + \bar{v}_{i+2})^2. \tag{2.17}$$

By performing the Taylor expansion at x_i, we have

$$\beta_1^{(1)} = \bar{v}_i'^2 \Delta x^2 + (\frac{13}{12}\bar{v}_i''^2 - \frac{2}{3}\bar{v}_i'\bar{v}_i''')\Delta x^4 - (\frac{13}{6}\bar{v}_i''\bar{v}_i''' - \frac{1}{2}\bar{v}_i'\bar{v}_i'''')\Delta x^5 + \mathcal{O}(\Delta x^6), \tag{2.18}$$

$$\beta_2^{(1)} = \bar{v}_i'^2 \Delta x^2 + (\frac{13}{12}\bar{v}_i''^2 + \frac{1}{3}\bar{v}_i'\bar{v}_i''')\Delta x^4 + \mathcal{O}(\Delta x^6), \tag{2.19}$$

$$\beta_3^{(1)} = \bar{v}_i'^2 \Delta x^2 + (\frac{13}{12}\bar{v}_i''^2 - \frac{2}{3}\bar{v}_i'\bar{v}_i''')\Delta x^4 + (\frac{13}{6}\bar{v}_i''\bar{v}_i''' - \frac{1}{2}\bar{v}_i'\bar{v}_i'''')\Delta x^5 + \mathcal{O}(\Delta x^6). \tag{2.20}$$

The linear weights $d_k(x)$ satisfy

$$p_5^C(x) = d_1(x)p_3^L(x) + d_2(x)p_3^C(x) + d_3(x)p_3^R(x) = v(x) + \mathcal{O}(\Delta x^5), \tag{2.21}$$

where $p_5^C(x)$ is defined by (2.25) in the following text. Afterwards, the nonlinear weights $w_k(x)$ are given by

$$\alpha_k(x) = \frac{d_k(x)}{(\epsilon + \beta_k^{(1)})^2}, w_k(x) = \frac{\alpha_k(x)}{\alpha_1(x) + \alpha_2(x) + \alpha_3(x)}, k = 1, 2, 3, \tag{2.22}$$

where the parameter ϵ is set as 10^{-6} to avoid the denominator becoming zero and reduce the influence of critical points. Then the WENO-JS reconstruction polynomial $P_1(x)$ is given by

$$P_1(x) = w_1(x)p_3^L(x) + w_2(x)p_3^C(x) + w_3(x)p_3^R(x). \tag{2.23}$$

2.3. The CWENOZ reconstruction

Next, we describe the central WENO type reconstruction method given in [66] which is used to solve steady-state problems. This WENO scheme was first named the WENO-ZQ scheme. In [12] (on page 2332, after Eqn. (7b)), it was pointed out that the WENO-ZQ scheme belongs to the central WENO class [5,11,12,30,31]. Thus, it will be termed as the CWENOZ scheme in the following text. In this paper, note that the term CWENOZ stresses the reconstruction method. More specifically, the numerical flux is evaluated at the cell boundary in this CWENOZ scheme instead of the midpoint of the cell originally. In the fifth-order case, for each of the following unequal-sized stencils

$$S_1^{(2)} = \{I_{i-2}, I_{i-1}, I_i, I_{i+1}, I_{i+2}\}, S_2^{(2)} = \{I_{i-1}, I_i\}, S_3^{(2)} = \{I_i, I_{i+1}\}, \tag{2.24}$$

there is a unique polynomial satisfying

$$\frac{1}{\Delta x}\int_{I_j} p_5^C(\xi)d\xi = \bar{v}_j, I_j \in S_1^{(2)}, \tag{2.25}$$

$$\frac{1}{\Delta x}\int_{I_j} p_2^L(\xi)d\xi = \bar{v}_j, I_j \in S_2^{(2)}, \tag{2.26}$$

$$\frac{1}{\Delta x}\int_{I_j} p_2^R(\xi)d\xi = \bar{v}_j, I_j \in S_3^{(2)}. \tag{2.27}$$

Let $(d_1, d_2, d_3) = (0.98, 0.01, 0.01)$ be the linear weights and let $\beta_1^{(2)}, \beta_2^{(2)}, \beta_3^{(2)}$ be the smoothness indicators of p_5^C, p_2^L, p_2^R respectively. Take

$$\tau = (\frac{|\beta_1^{(2)} - \beta_2^{(2)}| + |\beta_1^{(2)} - \beta_3^{(2)}|}{2})^2, \tag{2.28}$$

the nonlinear weights w_k are given by

$$\alpha_k = d_k(1 + \frac{\tau}{\epsilon + \beta_k^{(2)}}), w_k = \frac{\alpha_k}{\alpha_1 + \alpha_2 + \alpha_3}, k = 1, 2, 3. \tag{2.29}$$

Again, the parameter ϵ is set as 10^{-6} to avoid the denominator becoming zero and reduce the influence of critical points. The CWENOZ reconstruction polynomial $P_2(x)$ is given by

$$P_2(x) = \frac{w_1}{d_1}(p_5^C(x) - d_2 p_2^L(x) - d_3 p_2^R(x)) + w_2 p_2^L(x) + w_3 p_2^R(x). \tag{2.30}$$

2.4. The MRWENO reconstruction

Then, we describe the multi-resolution reconstruction method given in [69] that is also used to solve steady-state problems. This reconstruction procedure is termed as the MRWENO scheme in the following text. In the fifth-order case, for each of the following multi-level stencils

$$S_1^{(3)} = \{I_{i-2}, I_{i-1}, I_i, I_{i+1}, I_{i+2}\}, S_2^{(3)} = \{I_{i-1}, I_i, I_{i+1}\}, S_3^{(3)} = \{I_i\}, \tag{2.31}$$

there is a unique polynomial satisfying

$$\frac{1}{\Delta x}\int_{I_j} p_5^C(\xi)d\xi = \bar{v}_j, I_j \in S_1^{(3)}, \tag{2.32}$$

$$\frac{1}{\Delta x}\int_{I_j} p_3^C(\xi)d\xi = \bar{v}_j, I_j \in S_2^{(3)}, \tag{2.33}$$

$$\frac{1}{\Delta x}\int_{I_j} p_1^C(\xi)d\xi = \bar{v}_j, I_j \in S_3^{(3)}. \tag{2.34}$$

Let γ_{l,l_2} for $l = 1, \cdots, l_2$ and $l_2 = 2, 3$ be the linear weights, and they are set as $\gamma_{l,l_2} = \frac{\bar{\gamma}_{l,l_2}}{\sum_{l=1}^{l_2}\bar{\gamma}_{l,l_2}}$, in which $\bar{\gamma}_{1,2} = 1, \bar{\gamma}_{2,2} = 10$ and $\bar{\gamma}_{1,3} = 1, \bar{\gamma}_{2,3} = 10, \bar{\gamma}_{3,3} = 100$. Borrowing the similar idea from the CWENO schemes [5,11,12,30,31,66], denote

$$q_1(x) = p_1^C(x), \tag{2.35}$$

$$q_2(x) = \frac{1}{\gamma_{2,2}} p_3^C(x) - \frac{\gamma_{1,2}}{\gamma_{2,2}} q_1(x), \tag{2.36}$$

$$q_3(x) = \frac{1}{\gamma_{3,3}} p_5^C(x) - \frac{1}{\gamma_{3,3}}(\gamma_{1,3} q_1(x) + \gamma_{2,3} q_2(x)). \tag{2.37}$$

Let $\beta_2^{(3)}, \beta_3^{(3)}$ be the smoothness indicators of $q_2(x), q_3(x)$ respectively, which are computed by (2.14). Instead of setting $\beta_1^{(3)} = 0$, the choice of the smoothness indicator of $q_1(x)$ is quite different. Denote

$$\zeta_0 = (\bar{v}_i - \bar{v}_{i-1})^2, \zeta_1 = (\bar{v}_i - \bar{v}_{i+1})^2, \tag{2.38}$$

$$\bar{\gamma}_{0,1} = \begin{cases} 1, & \zeta_0 \geq \zeta_1, \\ 10, & otherwise, \end{cases} \quad \bar{\gamma}_{1,1} = 11 - \bar{\gamma}_{0,1}, \tag{2.39}$$

$$\gamma_{0,1} = \frac{\bar{\gamma}_{0,1}}{\bar{\gamma}_{0,1} + \bar{\gamma}_{1,1}}, \gamma_{1,1} = 1 - \gamma_{0,1}, \tag{2.40}$$

$$\sigma_0 = \gamma_{0,1}(1 + \frac{|\zeta_0 - \zeta_1|^2}{\zeta_0 + \epsilon}), \sigma_1 = \gamma_{1,1}(1 + \frac{|\zeta_0 - \zeta_1|^2}{\zeta_1 + \epsilon}), \sigma = \sigma_0 + \sigma_1, \tag{2.41}$$

where $\epsilon = 10^{-6}$ is added to avoid the denominator becoming zero and reduce the influence of critical points. Then, take

$$\beta_1^{(3)} = \frac{1}{\sigma^2}(\sigma_0(\bar{v}_i - \bar{v}_{i-1}) + \sigma_1(\bar{v}_{i+1} - \bar{v}_i))^2. \tag{2.42}$$

Set

$$\tau_3 = (\frac{|\beta_3^{(3)} - \beta_1^{(3)}| + |\beta_3^{(3)} - \beta_2^{(3)}|}{2})^2. \tag{2.43}$$

The nonlinear weights $w_{l,3}$ are given by

$$\alpha_{l,3} = \gamma_{l,3}(1 + \frac{\tau_3}{\epsilon + \beta_l^{(3)}}), w_{l,3} = \frac{\alpha_{l,3}}{\alpha_{1,3} + \alpha_{2,3} + \alpha_{3,3}}, l = 1, 2, 3. \tag{2.44}$$

The parameter ϵ is set as 10^{-6} as before to avoid the denominator becoming zero and reduce the influence of critical points. The MRWENO reconstruction polynomial $P_3(x)$ is given by

$$P_3(x) = \sum_{l=1}^{3} w_{l,3} q_l(x). \tag{2.45}$$

In any case mentioned above, the final fifth-order approximations at cell boundaries are given by

$$v^-_{i+\frac{1}{2}} = P_k(x_{i+\frac{1}{2}}), v^+_{i-\frac{1}{2}} = P_k(x_{i-\frac{1}{2}}), k = 1, 2, 3. \tag{2.46}$$

In the finite difference method, the numerical fluxes are taken as $\hat{f}^+_{i+\frac{1}{2}} = v^-_{i+\frac{1}{2}}$ by identifying $\bar{v}_i = f^+(u_i)$, and $\hat{f}^-_{i+\frac{1}{2}} = v^+_{i+\frac{1}{2}}$ with $\bar{v}_i = f^-(u_i)$.

3. The hybrid reconstruction method

This section proposes a new hybrid strategy to perform the reconstruction. The major difference from existing hybrid strategies is that the domain is classified into three parts: smooth, non-smooth, and transition regions. The high-order linear reconstruction is used in the smooth region, and the nonlinear WENO reconstruction is used in the non-smooth region. Meanwhile, a smooth transitive reconstruction connecting the reconstructions in smooth and non-smooth regions is adopted in the transition region for the steady-state convergence.

First, we need to propose a specific smoothness detector to identify the current stencil. There are many different ways to give the smoothness detectors in the hybrid methods. In this paper, we still adopt the smoothness indicator (2.14) as the primary ingredient in the smoothness detector as in [52]. This approach may not be the sharpest but a practical and straightforward choice.

For the fifth-order method, let $\tau_5 = |\beta_1^{(1)} - \beta_3^{(1)}|$ and $\beta^M = \frac{1}{3}\sum_{i=1}^{3}\beta_i^{(1)}$. In the smooth region, basically we have $\tau_5 < \beta^M$ since $\tau_5 = \mathcal{O}(\Delta x^5)$, and $\beta^M = \mathcal{O}(\Delta x^2)$ if there is no critical point. Define the **smoothness detector** $\eta = \frac{\tau_5}{\epsilon + \beta^M}$, where ϵ is set as 10^{-6} to reduce the influence of critical points and avoid the denominator becoming zero. The smooth region is identified by $\eta \le \frac{1}{2}$, the non-smooth region is identified by $\eta \ge 1$, and the transition region is identified by $\frac{1}{2} < \eta < 1$.

For the "smooth" region ($\eta \le \frac{1}{2}$), we adopt the linear reconstruction in (2.25), denoted by $P^A(x) = p_5^C(x)$. Next, we will introduce the reconstruction in the non-smooth and transition regions respectively.

3.1. Reconstruction in the non-smooth region

In the "non-smooth" region ($\eta \ge 1$), a blending technique of the linear and nonlinear reconstruction methods is proposed to increase the spectral resolution and the steady-state convergence, and maintain the ENO property.

First, we consider the stencils (2.24) used in the CWENOZ reconstruction. Similar to the procedures in the CWENOZ reconstruction, but now let $(d_1, d_2, d_3) = (1 - 2d, d, d)$ be the linear weights. Take

$$\tau = (\frac{|\beta_1^{(2)} - \beta_2^{(2)}| + |\beta_1^{(2)} - \beta_3^{(2)}|}{2})^2. \tag{3.1}$$

The nonlinear weights w_k are given by

$$\alpha_k = d_k(1 + \frac{\tau}{(\epsilon + \beta_k^{(2)})C_R}), w_k = \frac{\alpha_k}{\alpha_1 + \alpha_2 + \alpha_3}, k = 1, 2, 3. \tag{3.2}$$

The parameter ϵ is set as 10^{-6} to avoid the denominator becoming zero and reduce the influence of critical points. A typical choice of C_R is $C_R = 1$. However, this choice seems to cause some oscillations near discontinuities. For the sake of reducing the linearity of this reconstruction, we take

$$C_R = C_s \Delta x + \beta_* + C_b, \tag{3.3}$$

where C_b can be set, e.g., as 0.01 to avoid C_R becoming too small on very fine grids, and the scaling parameter C_s is defined by

$$C_s = (\sum_{j=i-2}^{i+2} |U_j|)^2, \tag{3.4}$$

where U_j is the point value of the variable under reconstruction. β_* is added to measure the smoothness of the five-point stencil, which can be set as $\beta_1^{(2)}$ or β^M, etc. In the formula of C_R, the first two terms dominate on coarse grids. When the grid is fine enough, the last two terms begin to dominate to provide proper linearity for steady-state convergence. In practice, if one finds that the residue in a small region only hangs at a relatively high level, C_b can be tuned to a larger number to improve the steady-state convergence. In all numerical tests in Sec. 4, C_b is chosen as 0.01 and β_* is set as $\beta_1^{(2)}$.

Afterwards, a WENO reconstruction polynomial $P^N(x)$ is given by

$$P^N(x) = w_1 p_5^C(x) + w_2 p_2^L(x) + w_3 p_2^R(x), \tag{3.5}$$

where $p_5^C(x)$, $p_2^L(x)$, $p_2^R(x)$ are given by (2.25)-(2.27).

Next, in order to further the spectral resolution of the scheme, we adopt an additional procedure to amplify its smoothness indicator as in [52]. Instead of $P^N(x)$, the following blending polynomial

$$P^C(x) = W_1 P^L(x) + W_2 P^N(x), \tag{3.6}$$

is applied in the non-smooth region, where the polynomial $P^L(x)$ is given by

$$P^L(x) = d_1 p_5^C(x) + d_2 p_2^L(x) + d_3 p_2^R(x). \tag{3.7}$$

This blending approximation is the convex combination of the $P^L(x)$ and $P^N(x)$ with the weights W_1 and W_2 respectively. The weights are computed by

$$W_1 = \min(1, \frac{1+\sqrt{1+(a+1)(Q-1)}}{a+1}),\ W_2 = 1 - W_1, \tag{3.8}$$

where $a = \frac{\beta^L}{\beta^A + 10^{-40}}$, $\beta^A = \min\{\beta_1^{(2)}, \beta_2^{(2)}, \beta_3^{(2)}\}$. By adopting this pair of weights (W_1, W_2), we can make a conclusion that the smoothness indicator of the blending polynomial $P^C(x)$ is no more than $2Q\beta^N$, where β^N is the smoothness indicator of $P^N(x)$. It can be justified as follows.

The smoothness indicator β^L of $P^L(x)$ can be computed by (2.14). To save computational cost, β^L can also be computed according to $\beta_1^{(2)}$ as follows

$$\beta^L = |d^2(\bar{v}_{i+1} - \bar{v}_{i-1})^2 + \frac{d(1-2d)(\bar{v}_{i+1} - \bar{v}_{i-1})(8\bar{v}_{i+1} - \bar{v}_{i+2} - 8\bar{v}_{i-1} + \bar{v}_{i-2})}{6} + (1-2d)^2 \beta_1^{(2)}|, \tag{3.9}$$

where d is the linear weight of lower order polynomials. Note that the absolute value should be taken to avoid β^L becoming negative caused by floating-point errors. The smoothness indicator of the blending polynomial $P^C(x)$ can be written as

$$\beta^C = \sum_{j=1}^{4} \Delta x^{2j-1} \int_{x_{i-\frac{1}{2}}}^{x_{i+\frac{1}{2}}} ((W_1 P^L + W_2 P^N)^{(j)})^2 dx, \tag{3.10}$$

thus we have

$$\beta^C \le 2 \sum_{j=1}^{4} \Delta x^{2j-1} \int_{x_{i-\frac{1}{2}}}^{x_{i+\frac{1}{2}}} ((W_1 P^L)^{(j)})^2 + ((W_2 P^N)^{(j)})^2 dx = 2(W_1^2 \beta^L + W_2^2 \beta^N). \tag{3.11}$$

We will get $\beta^C \le 2Q\beta^N$ as long as $2(W_1^2\beta^L + W_2^2\beta^N) \le 2Q\beta^N$. Since $\beta^A \le \beta^N$ and $a = \frac{\beta^L}{\beta^A + 10^{-40}}$, it suffices to let

$$W_1^2 a + W_2^2 = Q. \tag{3.12}$$

Substitute W_2 with $1 - W_1$, the conclusion follows by solving an one variable quadratic equation

$$(a+1)W_1^2 - 2W_1 + 1 - Q = 0. \tag{3.13}$$

Denote $F(a, Q) = \frac{1+\sqrt{1+(a+1)(Q-1)}}{a+1}$. It can be seen that F is an increasing function of Q and a decreasing function of a, which can be adaptively adjusted according to the flow field information. When $a \le Q$, the weight $W_1 = 1$ since $F(Q, Q) = 1$, thus the linear approximation is dominant. Through the smoothness amplification factor Q, we can control the usage of linear approximation in the non-smooth region. Set $Q = 1 + \frac{K \min\{\beta_1^{(1)}, \beta_2^{(1)}, \beta_3^{(1)}\}}{\beta^A + 10^{-40}}$, where K is set as 3 to control β^C. Then from the above proof, we can conclude that $\beta^C \le 2(\beta^A + K \min\{\beta_1^{(1)}, \beta_2^{(1)}, \beta_3^{(1)}\})$.

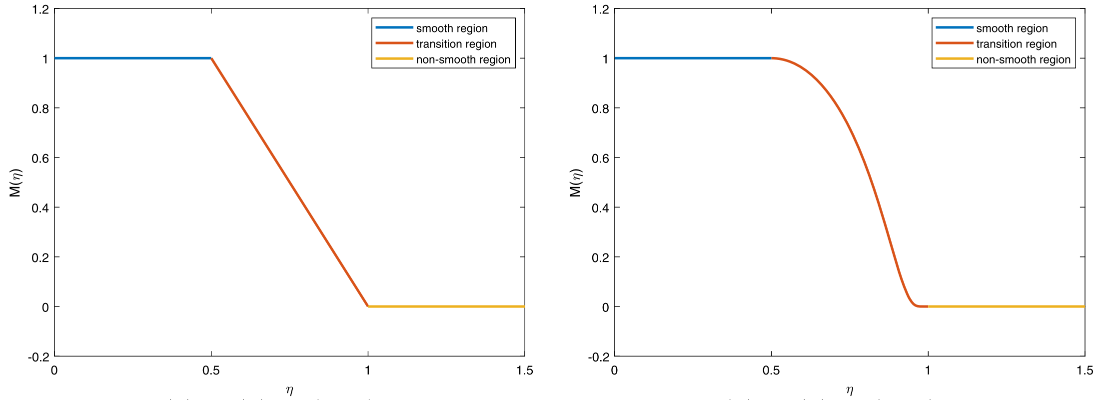

(a) $M(\eta)$ in (3.14) (b) $M(\eta)$ in (3.15)

Fig. 3.1. Illustration of the weight functions $M(\eta)$ in the transition region. (For interpretation of the colors in the figure(s), the reader is referred to the web version of this article.)

There are two motivations for adopting this blending reconstruction. First, the blending polynomial $P^C(x) = W_1 P^L(x) + W_2 P^N(x)$ gets closer to the linear polynomial $P^L(x)$ compared with the nonlinear polynomial $P^N(x)$, which may be helpful for steady-state convergence as pointed out in [66,69]. Second, the numerical dissipation is reduced a lot compared with the pure nonlinear reconstruction $P^N(x)$, as shown in the following numerical spectral analysis.

The blending polynomial $P^C(x) = \mu_1 p_5^C(x) + \mu_2 p_2^L(x) + \mu_3 p_2^R(x)$ can also be seen as a modified version of $P^N(x)$, with $\mu_1 = W_1 d_1 + W_2 w_1$, $\mu_2 = W_1 d_2 + W_2 w_2$, and $\mu_3 = W_1 d_3 + W_2 w_3$.

3.2. Reconstruction in the transition region

In the transition region ($\eta \in (\frac{1}{2}, 1)$), a smooth transitive reconstruction from the linear reconstruction to nonlinear reconstruction is introduced for steady-state convergence. The smoothing approximation in the transition region is the convex combination of the linear reconstruction $P^A(x)$ and the nonlinear reconstruction $P^C(x)$ with the weights $M(\eta)$ and $1 - M(\eta)$ based on the smoothness detector η, i.e. $P^B(x) = M(\eta)P^A(x) + (1 - M(\eta))P^C(x)$. The weight function $M(\eta)$ can be computed either by

$$M(\eta) = 2 - 2\eta, \ \eta \in (\frac{1}{2}, 1), \tag{3.14}$$

or

$$M(\eta) = e^{-\frac{(2\eta-1)^2}{1-(2\eta-1)^2}}, \ \eta \in (\frac{1}{2}, 1). \tag{3.15}$$

Fig. 3.1 illustrates the above choices of $M(\eta)$. In all the numerical tests, both weight functions perform well for the steady-state convergence. Thus, we only show the numerical results with the second weight function. Even though the weight function is not unique, it is essential for the steady-state convergence in our hybrid scheme.

Finally, we summarize our fifth-order hybrid reconstruction procedure as follows.

Algorithm 1 Procedure for the hybrid reconstruction.

procedure WENO-H
  Given the cell averages $\bar{v}_j$ for all j, calculate the smoothness detector η.
  if $\eta \le \frac{1}{2}$ **then**
    Perform the linear reconstruction: $P^A(x) = p_5^C(x)$
  else if $\frac{1}{2} < \eta < 1$ **then**
    Perform the transition reconstruction: $P^B(x) = M(\eta)P^A(x) + (1 - M(\eta))P^C(x)$
  else
    Perform the blending reconstruction: $P^C(x) = \mu_1 p_5^C(x) + \mu_2 p_2^L(x) + \mu_3 p_2^R(x)$

In this paper, the finite difference scheme based on this hybrid reconstruction is termed as the WENO-H scheme. To examine the performances of the schemes mentioned above, we adopt the approach in [39,42,43] to compare the approximate dispersion and dissipation relations with the fifth-order upwind linear (UW5) reconstruction and the popular fifth-order WENO-JS [28,38] reconstruction. Let ω, ω' be the reduced wave number and the modified wave number respectively. The parameter ϵ is set as 10^{-6} for all WENO schemes and the parameter C_b for the WENO-H scheme is set as 0.01. Besides, the linear weights for the CWENOZ scheme are set as $(d_1, d_2, d_3) = (0.98, 0.01, 0.01)$ as in [66], the linear weights for the

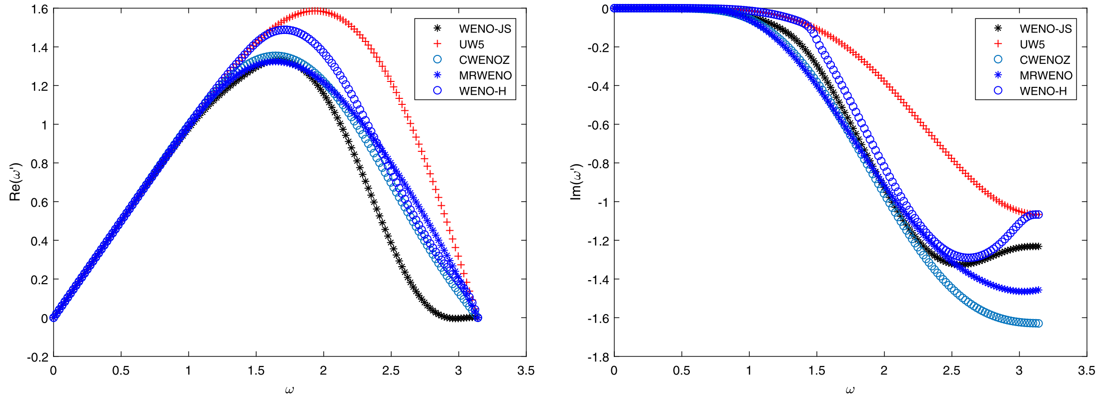

(a) Dispersion (b) Dissipation

Fig. 3.2. Approximate dispersion and dissipation relations for different schemes.

MRWENO scheme are set as $(\gamma_{1,3}, \gamma_{2,3}, \gamma_{3,3}) = (\frac{1}{111}, \frac{10}{111}, \frac{100}{111})$ as in [69], and linear weights for the WENO-H scheme are set as $(d_1, d_2, d_3) = (0.8, 0.1, 0.1)$. The results are shown in Fig. 3.2, which demonstrate that the new hybrid scheme maintains lower dissipative and dispersive errors than CWENOZ, MRWENO and WENO-JS schemes.

Remark 3.1. This hybrid strategy can also be applied to the MRWENO scheme, the second-order TVD scheme, and the first-order scheme, respectively, to construct new hybrid schemes to solve steady-state problems successfully. Expressly, with the same smoothness detector η, we can adopt the linear reconstruction in the smooth region, the MRWENO/TVD/P^0 blending reconstruction in the non-smooth region, and the smooth transitive reconstruction in the transition region. For the steady-state problems of Euler equations, these schemes work well for the steady-state convergence, at least in all our following numerical tests. For the brevity of the paper, we will not show the details.

4. Numerical tests

In this section, we present the numerical results of the fifth-order CWENOZ, MRWENO and WENO-H finite difference schemes for the steady-state problems of Euler equations. Since we adopt the pseudo-time marching approach, the third-order TVD/SSP Runge-Kutta method [20]

$$\begin{cases} \boldsymbol{u}^{(1)} = \boldsymbol{u}^n - \Delta t L(\boldsymbol{u}^n), \\ \boldsymbol{u}^{(2)} = \dfrac{3}{4}\boldsymbol{u}^n + \dfrac{1}{4}\boldsymbol{u}^{(1)} - \dfrac{1}{4}\Delta t L(\boldsymbol{u}^{(1)}), \\ \boldsymbol{u}^{n+1} = \dfrac{1}{3}\boldsymbol{u}^n + \dfrac{2}{3}\boldsymbol{u}^{(2)} - \dfrac{2}{3}\Delta t L(\boldsymbol{u}^{(2)}), \end{cases} \tag{4.1}$$

is used in the iterations, where L is the spatial discrete operator given by (2.4) or (2.6). Unless specified, the CFL number is set as 0.2 and the parameters set in all the numerical tests are the same as the choice in the approximate dispersion and dissipation relations analysis in the last section.

Let $R1_i, R2_i, R3_i, R4_i, R5_i$ be the local residue of five conservative variables for three-dimensional Euler equations (1.1), which are defined by $R1_i = \frac{\partial \rho}{\partial t}|_i \approx \frac{\rho_i^{n+1} - \rho_i^n}{\Delta t}$, $R2_i = \frac{\partial (\rho u)}{\partial t}|_i \approx \frac{(\rho u)_i^{n+1} - (\rho u)_i^n}{\Delta t}$, $R3_i = \frac{\partial (\rho v)}{\partial t}|_i \approx \frac{(\rho v)_i^{n+1} - (\rho v)_i^n}{\Delta t}$, $R4_i = \frac{\partial (\rho w)}{\partial t}|_i \approx \frac{(\rho w)_i^{n+1} - (\rho w)_i^n}{\Delta t}$, and $R5_i = \frac{\partial E}{\partial t}|_i \approx \frac{E_i^{n+1} - E_i^n}{\Delta t}$. Then the average residue is given by

$$Res_A = \sum_{i=1}^{N_D} \frac{|R1_i| + |R2_i| + |R3_i| + |R4_i| + |R5_i|}{(D+2)N_D}, \tag{4.2}$$

where N_D is the total number of grid points for one-dimensional or two-dimensional or three-dimensional problems and D is the dimension of space. In x or y or z direction, the maximum characteristic speed α in the Lax-Friedrichs flux splitting is typically set as $\max_{\Omega}(|u| + c)$ or $\max_{\Omega}(|v| + c)$ or $\max_{\Omega}(|w| + c)$ for each characteristic variable unless specified, where $c = \sqrt{\frac{\gamma P}{\rho}}$ $(\gamma = 1.4)$ is the sound speed and Ω is the whole computational domain. The legend "WENO(1.1)" indicates that the maximum characteristic speed α is amplified 1.1 times in this WENO scheme. For one-dimensional Euler equations, the time step is set as

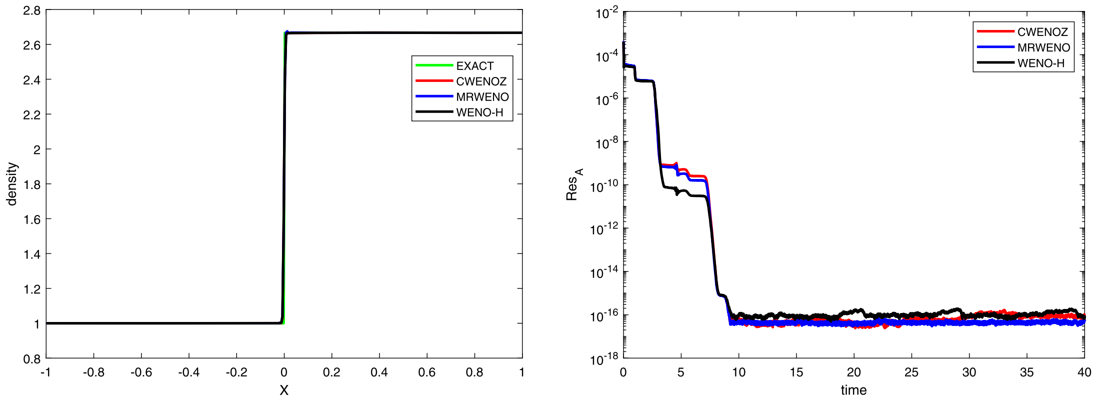

Fig. 4.1. Numerical results of Example 4.1 with 400 grid points. Left: density distributions of 1D stationary shock wave; right: the time history of average residue of different schemes.

$$\Delta t = \mathrm{CFL}\frac{\Delta x}{\max\limits_{\Omega}(|u|+c)}.$$

For two-dimensional Euler equations, the time step is chosen such that

$$\Delta t(\frac{\max\limits_{\Omega}(|u|+c)}{\Delta x}+\frac{\max\limits_{\Omega}(|v|+c)}{\Delta y})=\mathrm{CFL},$$

and three-dimensional Euler equations,

$$\Delta t(\frac{\max\limits_{\Omega}(|u|+c)}{\Delta x}+\frac{\max\limits_{\Omega}(|v|+c)}{\Delta y}+\frac{\max\limits_{\Omega}(|w|+c)}{\Delta z})=\mathrm{CFL}.$$

Example 4.1. As the first example, we consider the one-dimensional stationary shock wave. The governing equation takes the form

$$\frac{\partial \boldsymbol{F}(\boldsymbol{U})}{\partial x}=\mathbf{0}, \tag{4.3}$$

where $\boldsymbol{U}=(\rho,\rho u,E)^T$ and $\boldsymbol{F}(\boldsymbol{U})=(\rho u,\rho u^2+P,u(E+P))^T$. We compute this problem on the interval $[-1,1]$, and the shock wave is located at $x=0$. The Mach number of the left flow is set as $M_\infty=2$. The initial conditions are given by

$$\boldsymbol{U}(x,0)=\begin{cases}\boldsymbol{U}_L, x<0,\\ \boldsymbol{U}_R, x\ge 0,\end{cases} \tag{4.4}$$

where

$$\begin{pmatrix}P_L\\ \rho_L\\ u_L\end{pmatrix}=\begin{pmatrix}\frac{1}{\gamma M_\infty^2}\\ 1\\ 1\end{pmatrix},\ \begin{pmatrix}P_R\\ \rho_R\\ u_R\end{pmatrix}=\begin{pmatrix}P_L\frac{2\gamma M_\infty^2-(\gamma-1)}{\gamma+1}\\ \frac{\frac{\gamma+1}{\gamma-1}\frac{P_R}{P_L}+1}{\frac{\gamma+1}{\gamma-1}+\frac{P_R}{P_L}}\\ \sqrt{\gamma\frac{(2+(\gamma-1)M_\infty^2)P_R}{(2\gamma M_\infty^2+(1-\gamma))\rho_R}}\end{pmatrix}.$$

We present the results when the numerical solutions have reached their steady states. The density distributions of the numerical solutions are shown in Figs. 4.1 and 4.2. From the zoom-in Fig. 4.2, we can see that the result of the WENO-H scheme is less oscillatory. We also show the time history of the average residue of different schemes in Fig. 4.1. It can be seen that the average residue of all schemes can settle down to machine zero.

Example 4.2. As an accuracy test, we consider the following two-dimensional Euler equations with source terms

$$\frac{\partial}{\partial x}\begin{pmatrix}\rho u\\ \rho u^2+P\\ \rho uv\\ u(E+P)\end{pmatrix}+\frac{\partial}{\partial y}\begin{pmatrix}\rho v\\ \rho uv\\ \rho v^2+P\\ v(E+P)\end{pmatrix}=\begin{pmatrix}0.4\cos(x+y)\\ 0.6\cos(x+y)\\ 0.6\cos(x+y)\\ 1.8\cos(x+y)\end{pmatrix}. \tag{4.5}$$

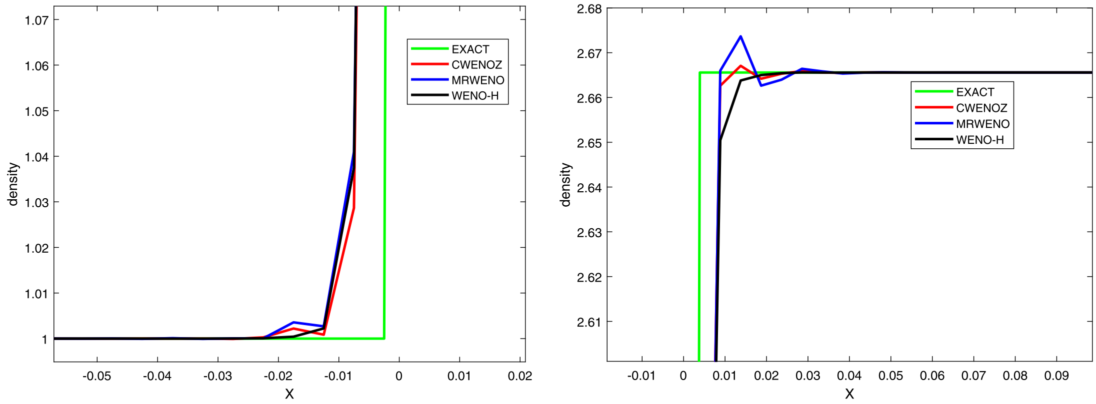

Fig. 4.2. Numerical results of Example 4.1 with 400 grid points. Left: zoom-in picture around the left of shock wave; right: zoom-in picture around the right of shock wave.

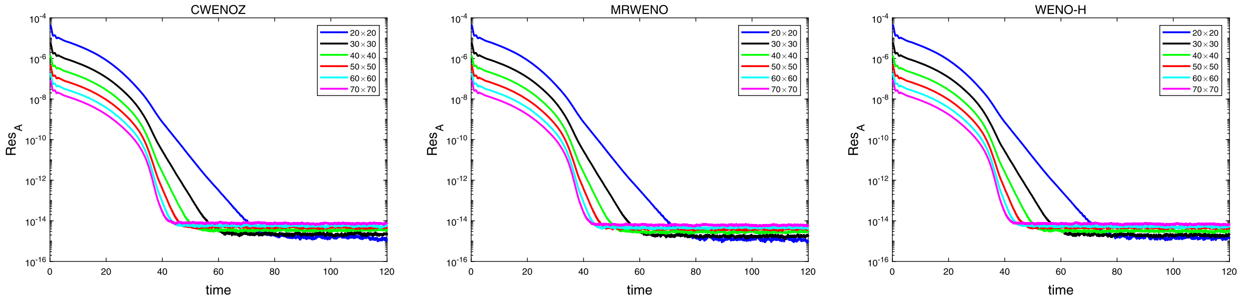

Fig. 4.3. Average residue history of different schemes for Example 4.2. Left: the CWENOZ scheme; center: the MRWENO scheme; right: the WENO-H scheme.

Table 4.1
L^1 and L^∞ errors of different schemes for Example 4.2. Steady state.

$N_x \times N_y$	UW5				WENO-H			
	L^1 error	order	L^∞ error	order	L^1 error	order	L^∞ error	order
20 × 20	1.86E-03	––	1.25E-04	––	1.86E-03	––	1.25E-04	––
30 × 30	2.51E-04	4.94	1.61E-05	5.05	2.51E-04	4.94	1.61E-05	5.05
40 × 40	6.01E-05	4.97	3.71E-06	5.11	6.01E-05	4.97	3.71E-06	5.11
50 × 50	1.98E-05	4.98	1.19E-06	5.09	1.98E-05	4.98	1.19E-06	5.09
60 × 60	7.96E-06	4.99	4.81E-07	4.98	7.96E-06	4.99	4.81E-07	4.98
70 × 70	3.69E-06	4.99	2.23E-07	4.97	3.69E-06	4.99	2.23E-07	4.97

The exact steady-state solutions are $\rho(x, y) = 1 + 0.2\sin(x + y), u(x, y) = 1, v(x, y) = 1$, and $P(x, y) = 1 + 0.2\sin(x + y)$. The initial solutions are set as the exact solutions projected onto the grid. We compute this problem in a square domain $[0, 2\pi] \times [0, 2\pi]$, and the boundary conditions of all the directions are imposed by the exact solutions. We show the time history of the average residue in Fig. 4.3. It shows that the residue of all schemes settles down to tiny values close to machine zero. The accuracy test results are listed in Table 4.1, and the final computational time is $T = 120$. The results of the CWENOZ and MRWENO schemes are omitted for simplicity since they are similar to the result of the WENO-H scheme. We can see that the WENO-H scheme achieves the designed fifth-order accuracy.

Example 4.3. Then we consider the 2D vortex evolution problem. We compute this nonlinear problem on a square $[0, 10]^2$ with periodic boundary condition. The mean flow is $\rho = 1, P = 1, (u, v) = (1, 1)$. An isentropic vortex is added with no perturbation in the entropy $S = \frac{P}{\rho^\gamma}$. Take temperature $T_s = \frac{P}{\rho}$, and the perturbation for the velocities (u, v), T_s, S can be given as follows:

$$(\delta u, \delta v) = \frac{\epsilon}{2\pi} e^{0.5(1-r^2)}(-\bar{y}, \bar{x}),\ \delta T_s = -\frac{(\gamma-1)\epsilon^2}{8\gamma\pi^2} e^{1-r^2},\ \delta S = 0, \tag{4.6}$$

where $(\bar{x}, \bar{y}) = (x-5, y-5)$, $r^2 = \bar{x}^2 + \bar{y}^2$, and the vortex strength is set as $\epsilon = 5$. The exact solution is the passive convection of the vortex with the mean velocity. As an accuracy test, we solve the unsteady Euler equations

Table 4.2
L^1 and L^∞ errors of different schemes for Example 4.3.

$N_x \times N_y$	UW5				WENO-H			
	L^1 error	order	L^∞ error	order	L^1 error	order	L^∞ error	order
10×10	2.97E-01	——	6.36E-02	——	3.71E-01	——	7.87E-02	——
20×20	3.52E-02	3.08	5.62E-03	3.50	4.85E-02	2.94	1.36E-02	2.53
40×40	1.77E-03	4.32	2.73E-04	4.36	2.42E-03	4.33	4.98E-04	4.77
80×80	6.33E-05	4.80	1.01E-05	4.76	2.22E-04	3.45	9.31E-05	2.42
160×160	2.12E-06	4.90	3.20E-07	4.98	2.12E-06	6.71	3.19E-07	8.19
320×320	8.34E-08	4.67	1.30E-08	4.62	8.34E-08	4.67	1.30E-08	4.62
$N_x \times N_y$	MRWENO				CWENOZ			
	L^1 error	order	L^∞ error	order	L^1 error	order	L^∞ error	order
10×10	5.05E-01	——	1.06E-01	——	5.03E-01	——	1.01E-01	——
20×20	6.41E-02	2.98	2.19E-02	2.27	6.43E-02	2.97	2.72E-02	1.89
40×40	1.86E-03	5.11	7.79E-04	4.81	2.01E-03	5.00	7.38E-04	5.20
80×80	6.33E-05	4.88	1.07E-05	6.19	6.34E-05	4.99	1.06E-05	6.12
160×160	2.12E-06	4.90	3.20E-07	5.06	2.12E-06	4.90	3.19E-07	5.05
320×320	8.35E-08	4.67	1.30E-08	4.63	8.34E-08	4.67	1.30E-08	4.62

$$\frac{\partial}{\partial t}\begin{pmatrix}\rho\\ \rho u\\ \rho v\\ E\end{pmatrix}+\frac{\partial}{\partial x}\begin{pmatrix}\rho u\\ \rho u^2+P\\ \rho uv\\ u(E+P)\end{pmatrix}+\frac{\partial}{\partial y}\begin{pmatrix}\rho v\\ \rho uv\\ \rho v^2+P\\ v(E+P)\end{pmatrix}=\mathbf{0}, \tag{4.7}$$

and the final computational time is $T = 0.2$. We take $\Delta t \approx \Delta x^{\frac{5}{3}}$ to make sure that the spatial error dominates, the numerical results are shown in Table 4.2. We can observe that all schemes achieve the designed fifth-order accuracy.

Example 4.4. Next we consider the shock reflection problem. We compute this problem in a rectangular $[0, 4] \times [0, 1]$. The reflection boundary condition and the supersonic outflow boundary condition are applied along the bottom boundary and right boundary respectively. The boundary conditions on other two sides are given by

$$(\rho, u, v, P)^T = \begin{cases}(1.0, 2.9, 0, \dfrac{1.0}{1.4})^T|_{(0,y,t)^T},\\ (1.69997, 2.61934, -0.50632, 1.52819)^T|_{(x,1,t)^T}.\end{cases} \tag{4.8}$$

The initial condition is equal to that at the left boundary. The time history of the average residue is shown in Fig. 4.4, from which we see that only the average residue of the WENO-H scheme could settle down to a tiny value, around 10^{-12}. To further verify the robustness and good convergence of the new scheme, we take $\varepsilon = 10^{-10}$ to compute this case. The result is also shown in Fig. 4.4. We can see that the residue can still converge to a tiny value. As an alternative choice, taking x direction for example, the maximum characteristic speeds can be set as $\max_\Omega |u-c|, \max_\Omega |u|, \max_\Omega |u|, \max_\Omega |u| + c$ respectively for the four characteristic variables. By adopting this choice of maximum characteristic speeds, the time history of the average residue is shown in Fig. 4.5, from which now we can observe that the average residue of all WENO schemes could settle down to a tiny value around 10^{-12}. The density contours of the numerical solutions after steady states reached are presented in Fig. 4.6, and the density distributions along the line $y = 0.5 - \frac{\Delta y}{2}$ are shown in Fig. 4.5. It can be seen that some oscillations appear in the numerical solutions of the CWENOZ and MRWENO schemes. In contrast, the numerical solution of the WENO-H scheme achieves the essentially non-oscillation property better.

Example 4.5. Next, we consider the forward-facing step problem. The wind tunnel is three units in length and 1 unit in width. Initially, a Mach 3 flow with $(\rho, u, v, P)^T = (1.4, 3.0, 0, 1.0)^T$ goes from the left to the right. The step with a height of 0.2 units is located in the interval $[0.6, 3]$. Inflow and outflow boundary conditions are applied along the left and right boundaries, respectively, and reflective boundary conditions are imposed along the walls of the tunnel. Based on the assumption of a nearly steady flow, we adopt the method introduced in [55] to fix the singularity at the corner of the step. We show the results when the numerical solutions have arrived at their numerical steady states. The history of the average residue is shown in Fig. 4.7, which shows that the average residue of all schemes can settle down to a value around 10^{-13} except for the MRWENO scheme. But the MRWENO(1.1) scheme can solve this issue successfully. The density contours of the numerical solutions are presented in Fig. 4.8, and the density distributions along the line $y = 0.5 - \frac{\Delta y}{2}$ are also shown in Fig. 4.7. It can be seen that all schemes can solve this problem well now. Note that this is not a pure steady-state problem since the slip line will appear when the grid is fine enough.

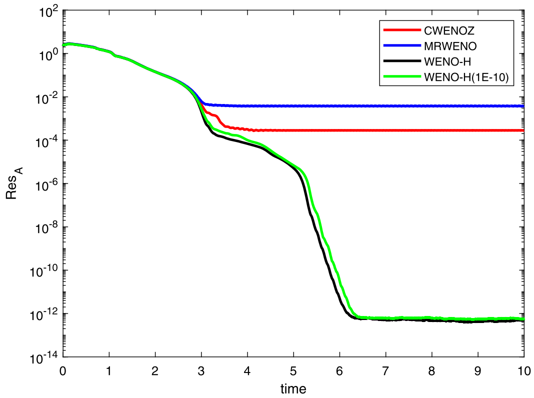

Fig. 4.4. The time history of average residue of different schemes for Example 4.4 with mesh size 120 × 30.

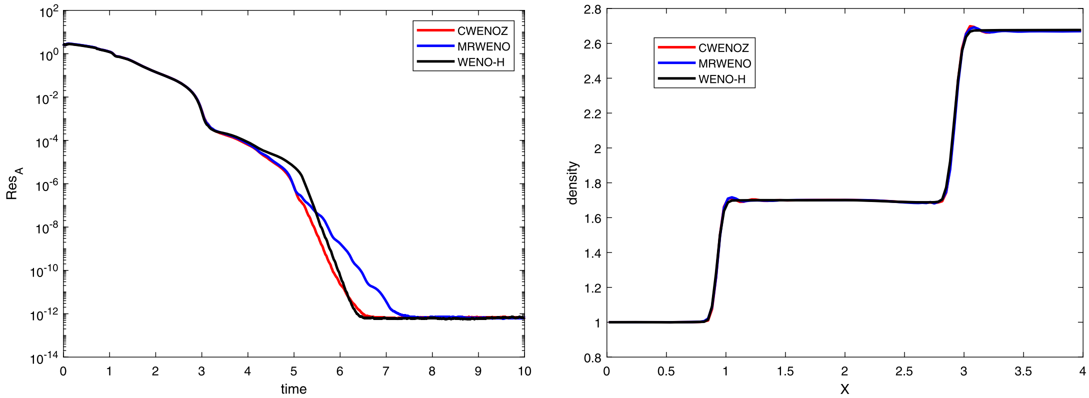

Fig. 4.5. Numerical results of Example 4.4 with mesh size 120 × 30. Left: the history of average residue of different schemes; right: 1D cut along $y = 0.5 - \frac{\Delta y}{2}$ for different schemes.

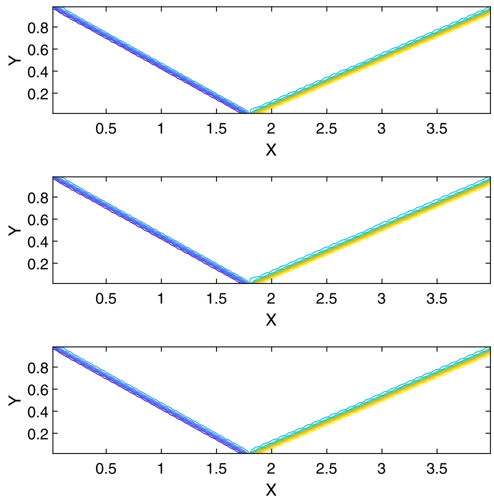

Fig. 4.6. Density contours of different schemes for Example 4.4 with mesh size 120 × 30. 15 equally spaced contour lines from 1.10 to 2.58. Top: result of the CWENOZ scheme; center: result of the MRWENO scheme; bottom: result of the WENO-H scheme.

Example 4.6. A 2D supersonic flow past a cylinder [28]. The physical smooth grid is presented in Fig. 4.9. We compute this problem in the square $[0, 1]^2$ on the ξ-η plane. The transformations between the physical domain and the computational domain are

$$x = -(R_x - (R_x - 0.5)\xi)\cos(\theta(2\eta - 1)), \tag{4.9}$$

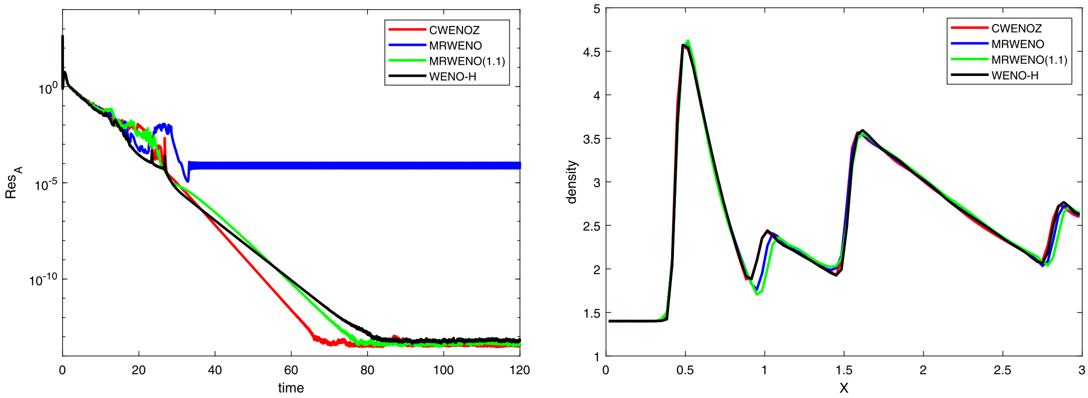

Fig. 4.7. Numerical results of Example 4.5 with mesh size 90×30. Left: the history of average residue of different schemes; right: 1D cut along $y = 0.5 - \frac{\Delta y}{2}$ for different schemes.

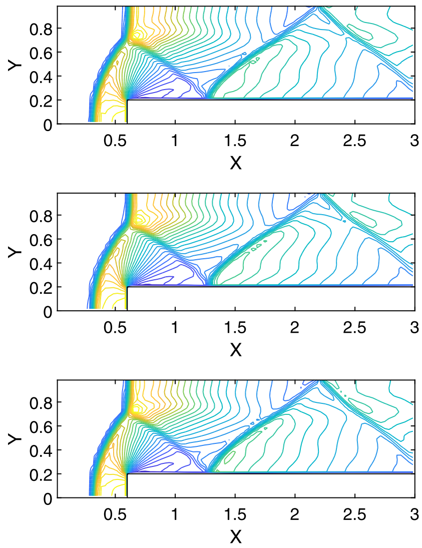

Fig. 4.8. Density contours of different schemes for Example 4.5 with mesh size 90×30. 30 equally spaced contour lines from 0.32 to 6.15. Top: result of the CWENOZ scheme; center: result of the MRWENO scheme; bottom: result of the WENO-H scheme.

and

$$y = (R_y - (R_y - 0.5)\xi)\sin(\theta(2\eta - 1)), \tag{4.10}$$

where $R_x = 3$, $R_y = 6$, and $\theta = \frac{\pi}{2}$. The initial condition is a Mach 3 flow with $(\rho, u, v, P) = (1.0, 3\sqrt{1.4}, 0, 1.0)$. The outflow boundary condition is applied at $\eta = 0$ and $\eta = 1$, and the inflow boundary condition is applied at $\xi = 0$. At $\xi = 1$, the reflective boundary condition is imposed. The time history of the average residue is presented in Fig. 4.10, which shows that the average residue of all schemes can settle down to a value around 10^{-14}, close to machine zero. The pressure contours of numerical solutions are shown in Fig. 4.11, and the pressure distributions along the line $\xi = \frac{5}{6} - \frac{\Delta\xi}{2}$ are also shown in Fig. 4.10. It can be seen that all schemes can solve this problem well, while the WENO-H scheme gives sharper resolution.

We proceed to solve this problem with mesh size 120×160. The time history of the average residue is presented in Fig. 4.12, which shows that only the average residue of the WENO-H scheme can settle down to the round-off error level. The pressure contours of numerical solutions are shown in Fig. 4.13, and the pressure distributions along the line $\xi = \frac{5}{6} - \frac{\Delta\xi}{2}$ are also shown in Fig. 4.12. Still the result of the WENO-H scheme looks sharper.

Example 4.7. A supersonic flow past a plate with angle $\theta = 15°$. The initial condition is given by $(\rho, u, v, P) = (1, \cos(\theta), \sin(\theta), \frac{1}{9\gamma})$, where $\gamma = 1.4$. We compute this problem in a square $[0, 10] \times [-5, 5]$. The plate is located at $[1, 2] \times \{0\}$, and the slip boundary condition is imposed on it. The inflow boundary condition is applied along the left and bottom boundaries, while the outflow boundary condition is applied along the right and top boundaries. We present the results when the numerical solutions have reached their steady states. First, we compute this problem with mesh size

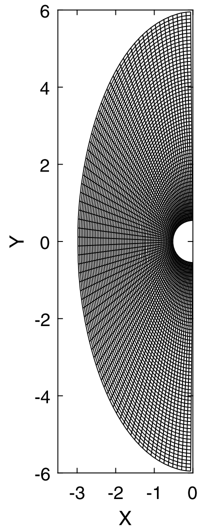

Fig. 4.9. The 2D supersonic flow past a cylinder problem for Example 4.6. The physical grid with mesh size 60×80.

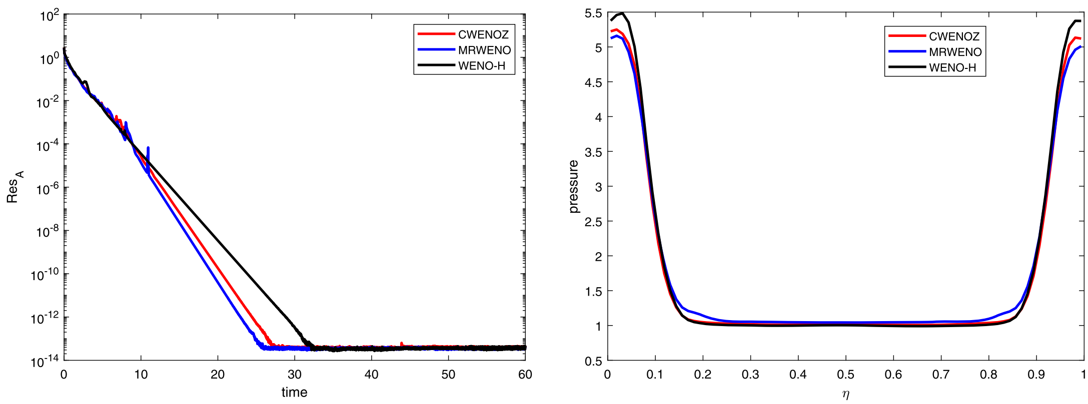

Fig. 4.10. Numerical results of Example 4.6 with mesh size 60×80. Left: the history of average residue of different schemes; right: 1D cut along $\xi = \frac{5}{6} - \frac{\Delta\xi}{2}$ for different schemes.

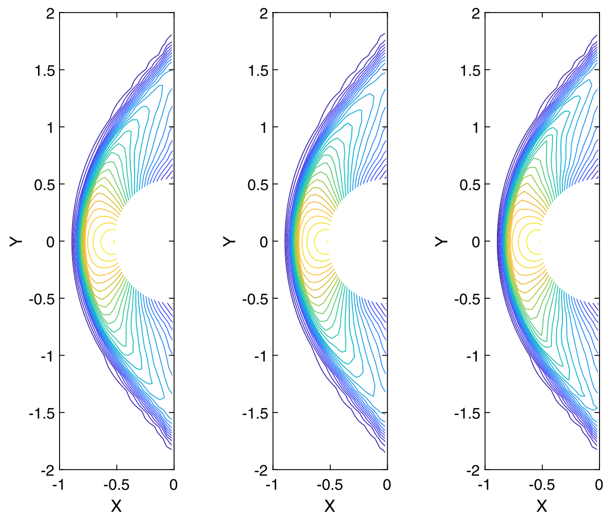

Fig. 4.11. Pressure contours of different schemes for Example 4.6 with mesh size 60×80. 30 equally spaced contour lines from 0.0 to 12.0. Left: result of the CWENOZ scheme; center: result of the MRWENO scheme; right: result of the WENO-H scheme.

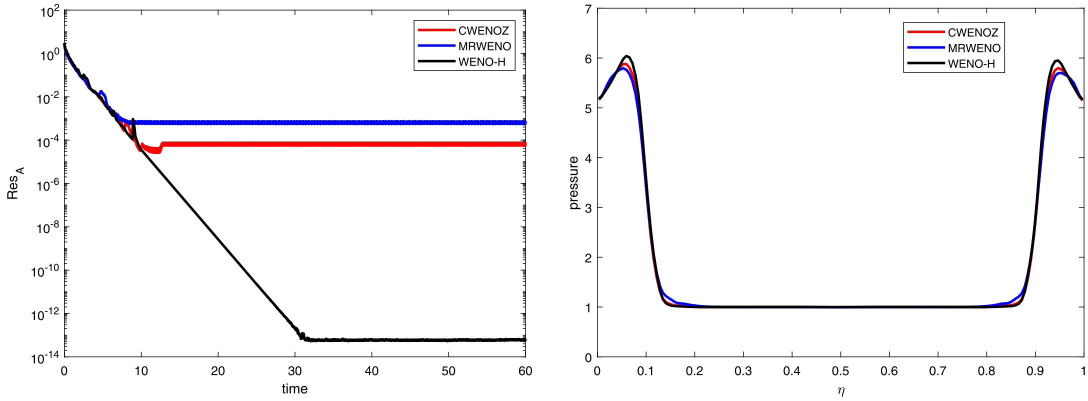

Fig. 4.12. Numerical results of Example 4.6 with mesh size 120×160. Left: the history of average residue of different schemes; right: 1D cut along $\xi = \frac{5}{6} - \frac{\Delta\xi}{2}$ for different schemes.

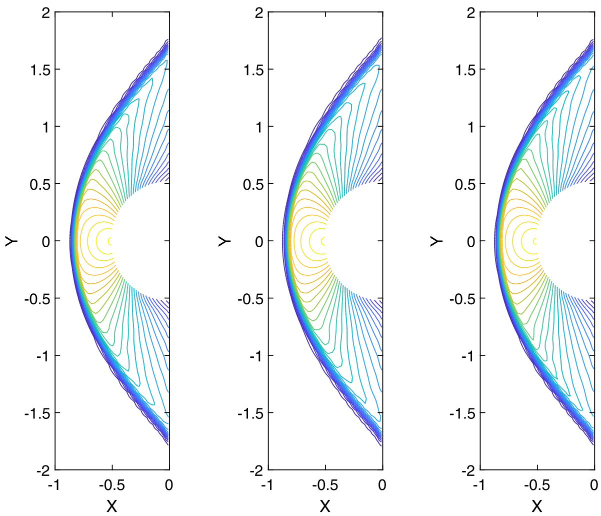

Fig. 4.13. Pressure contours of different schemes for Example 4.6 with mesh size 120×160. 30 equally spaced contour lines from 0.0 to 12.0. Left: result of the CWENOZ scheme; center: result of the MRWENO scheme; right: result of the WENO-H scheme.

200×200. The time history of the average residue is presented in Fig. 4.14, from which we can see that the average residue of all schemes can settle down to a value around $10^{-13.5}$. The pressure contours of the numerical solutions are shown in Fig. 4.15, from which we can see that the contours of the WENO-H scheme seem to be slightly sharper. The pressure distributions along the line $x = 8 - \frac{\Delta x}{2}$ are shown in Fig. 4.14. Thus, the hybrid one suppresses numerical oscillation better than the CWENOZ and MRWENO schemes.

Then we compute this problem with mesh size 400×400. The time history of the average residue is presented in Fig. 4.16. It can be seen that the average residue of both the CWENOZ scheme and the WENO-H scheme can settle down to a value around 10^{-13}, while the average residue of the MRWENO scheme only settles down to a value around $10^{-3.5}$. But this time MRWENO(1.1) scheme can not solve this issue either. Additionally, the residue of the WENO-H scheme is less than the residue of the CWENOZ scheme at any time in this example. The pressure contours of the numerical solutions are shown in Fig. 4.17, from which it seems that the contours of the WENO-H scheme are still sharp and clear. The pressure distributions along the line $x = 8 - \frac{\Delta x}{2}$ are also shown in Fig. 4.16. Obviously, the hybrid one suppresses numerical oscillation better than the CWENOZ and MRWENO schemes.

Example 4.8. A supersonic flow past two plates with angle $\theta = 15°$. The initial condition is given by $(\rho, u, v, P) = (1, \cos(\theta), \sin(\theta), \frac{1}{9\gamma})$, where $\gamma = 1.4$. We compute this problem in a square $[0, 10] \times [-5, 5]$. The first plate is located at $[2, 3] \times \{-2\}$, and the second plate is located at $[2, 3] \times \{2\}$. We impose the slip boundary condition on these plates. The inflow boundary condition is applied along the left and bottom boundaries, while the outflow boundary condition is applied along the right and top boundaries. We present the results when the numerical solutions have reached their steady states. First, we compute this problem with mesh size 200×200. The time history of the average residue is presented in Fig. 4.18.

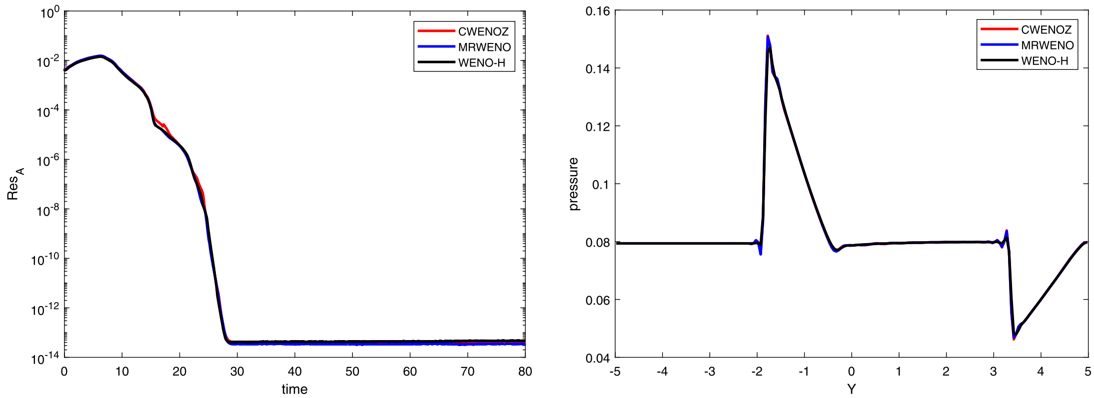

Fig. 4.14. Numerical results of Example 4.7 with mesh size 200×200. Left: the history of average residue of different schemes; right: 1D cut along $x = 8 - \frac{\Delta x}{2}$ for different schemes.

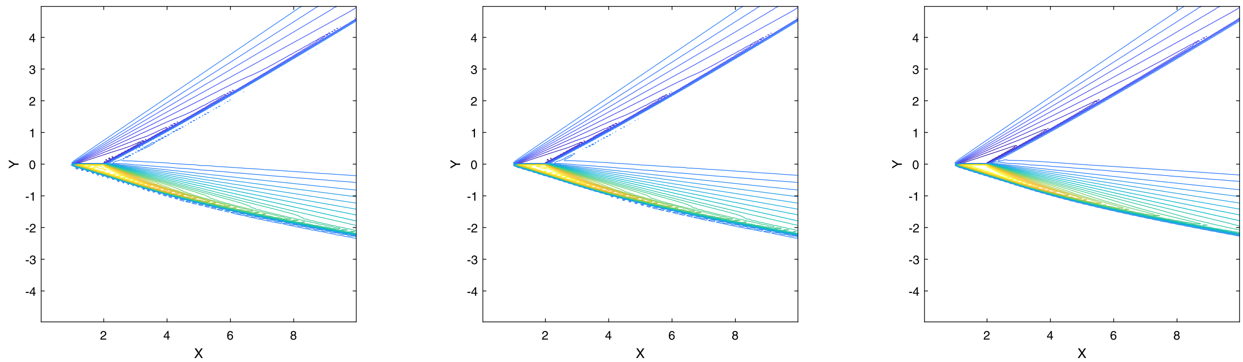

Fig. 4.15. Pressure contours of different schemes for Example 4.7 with mesh size 200×200. 30 equally spaced contour lines from 0.02 to 0.23. Left: result of the CWENOZ scheme; center: result of the MRWENO scheme; right: result of the WENO-H scheme.

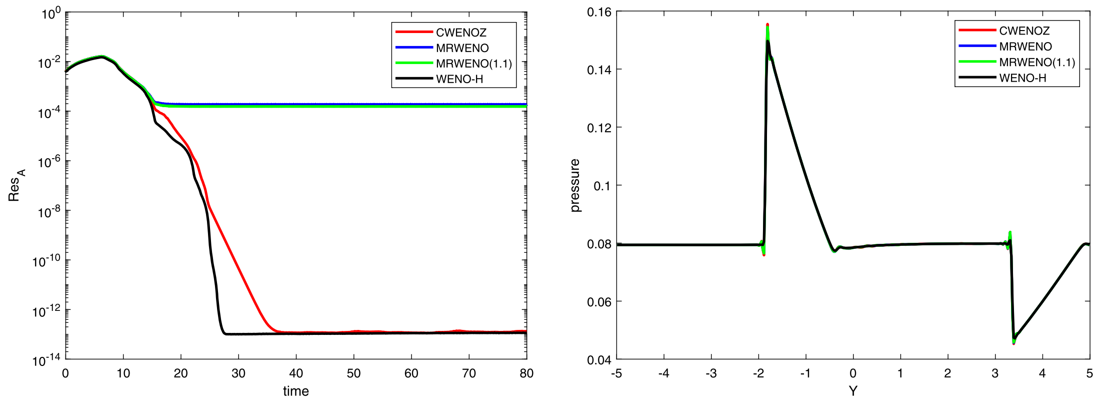

Fig. 4.16. Numerical results of Example 4.7 with mesh size 400×400. Left: the history of average residue of different schemes; right: 1D cut along $x = 8 - \frac{\Delta x}{2}$ for different schemes.

The average residue of all schemes can settle down to a tiny value around $10^{-13.5}$. The pressure contours of the numerical solutions are shown in Fig. 4.19. It can be found that the contours of the WENO-H scheme appear to be sharper than the other two. The pressure distributions along the line $x = 8 - \frac{\Delta x}{2}$ are also shown in Fig. 4.18, which shows that the hybrid one suppresses numerical oscillation better than the CWENOZ and MRWENO schemes.

Next, we compute this problem with mesh size 400×400. The time history of the average residue is presented in Fig. 4.20. But this time, we find that the average residue of both the CWENOZ scheme and the WENO-H scheme can settle down to a value around 10^{-13}, while the average residue of the MRWENO scheme only settles down to a value around $10^{-3.5}$. Besides, the residue of the hybrid one is less than the residue of the CWENOZ scheme at any time in this case. The pressure contours of the numerical solutions are shown in Fig. 4.21. It can also be observed that the contours of the

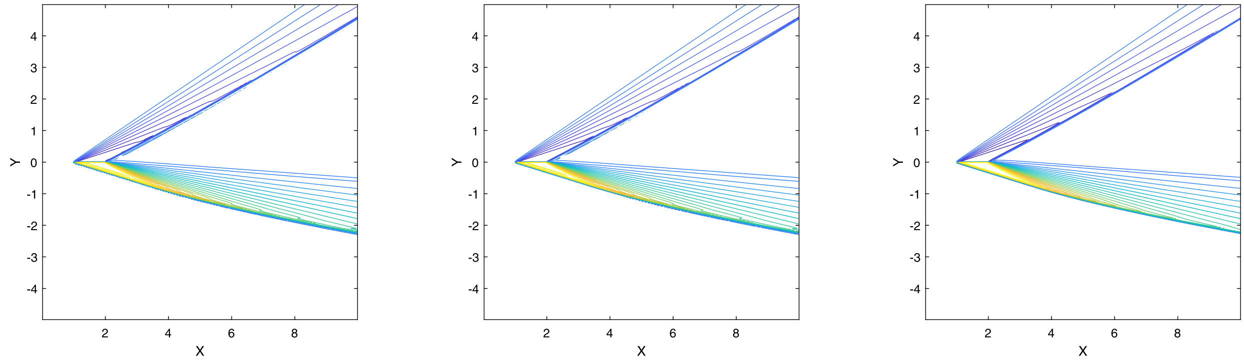

Fig. 4.17. Pressure contours of different schemes for Example 4.7 with mesh size 400 × 400. 30 equally spaced contour lines from 0.02 to 0.23. Left: result of the CWENOZ scheme; center: result of the MRWENO scheme; right: result of the WENO-H scheme.

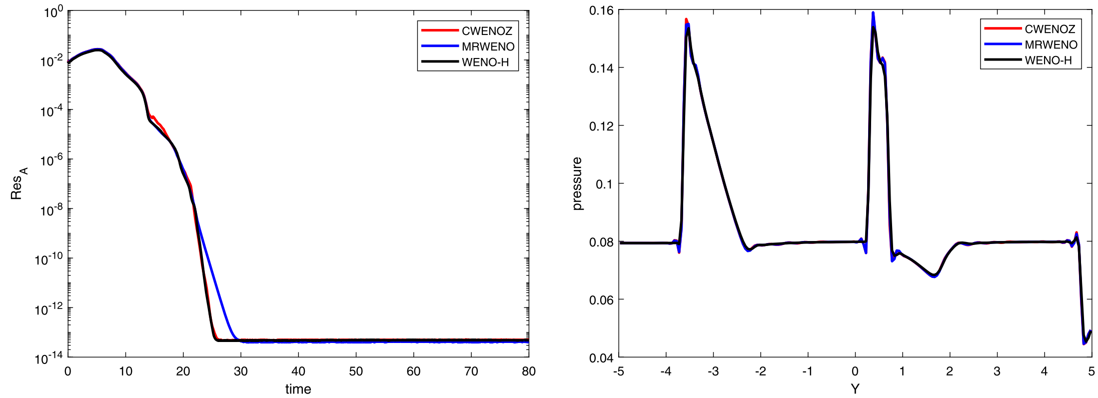

Fig. 4.18. Numerical results of Example 4.8 with mesh size 200 × 200. Left: the history of average residue of different schemes; right: 1D cut along $x = 8 - \frac{\Delta x}{2}$ for different schemes.

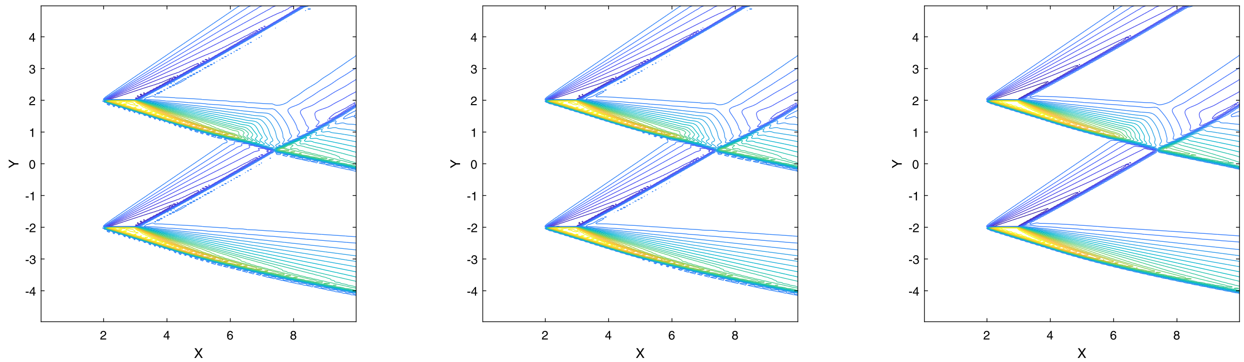

Fig. 4.19. Pressure contours of different schemes for Example 4.8 with mesh size 200 × 200. 30 equally spaced contour lines from 0.02 to 0.23. Left: result of the CWENOZ scheme; center: result of the MRWENO scheme; right: result of the WENO-H scheme.

WENO-H scheme look sharp and clear. The pressure distributions along the line $x = 8 - \frac{\Delta x}{2}$ are also shown in Fig. 4.20. Again, the hybrid one suppresses numerical oscillation better than the CWENOZ and MRWENO schemes.

Example 4.9. A supersonic flow past three plates with angle $\theta = 10°$. The initial condition is given by $(\rho, u, v, P) = (1, \cos(\theta), \sin(\theta), \frac{1}{9\gamma})$, where $\gamma = 1.4$. We compute this problem in a square $[0, 10] \times [-5, 5]$. The first plate is located at $[2, 3] \times \{-2\}$, the second plate is located at $[1, 2] \times \{0\}$, and the third plate is located at $[2, 3] \times \{2\}$. We impose the slip boundary condition on these plates. The inflow boundary condition is applied along the left and bottom boundaries, while the outflow boundary condition is applied along the right and top boundaries. We present the results when the numerical solutions have reached their steady states. The time history of the average residue is presented in Fig. 4.22. The average residue of all schemes can settle down to a value around 10^{-13}. The pressure contours of the numerical solutions are shown

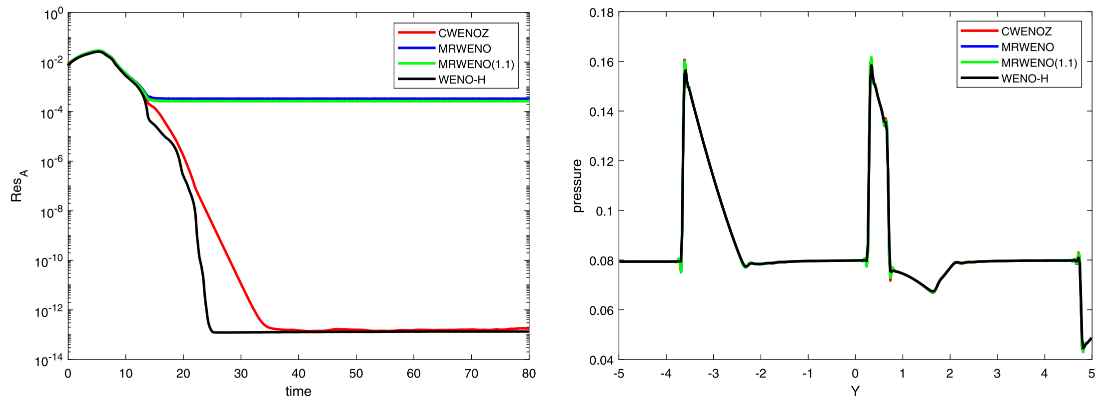

Fig. 4.20. Numerical results of Example 4.8 with mesh size 400 × 400. Left: the history of average residue of different schemes; right: 1D cut along $x = 8 - \frac{\Delta x}{2}$ for different schemes.

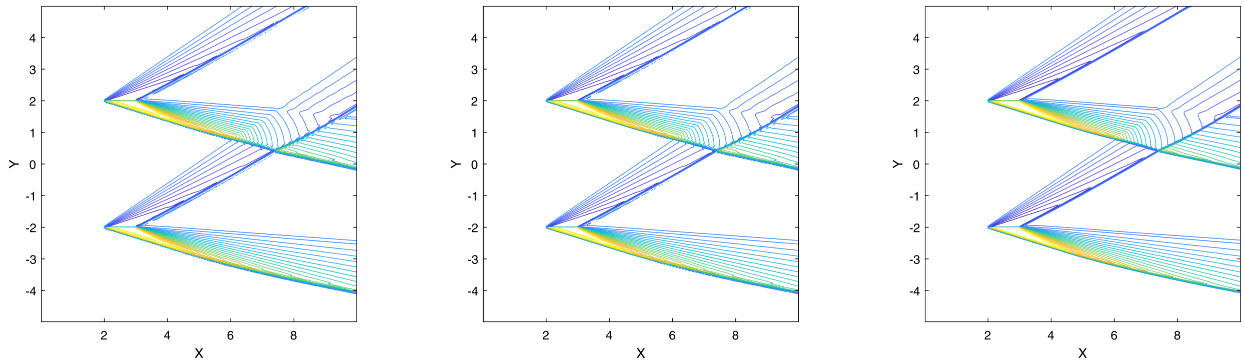

Fig. 4.21. Pressure contours of different schemes for Example 4.8 with mesh size 400 × 400. 30 equally spaced contour lines from 0.02 to 0.23. Left: result of the CWENOZ scheme; center: result of the MRWENO scheme; right: result of the WENO-H scheme.

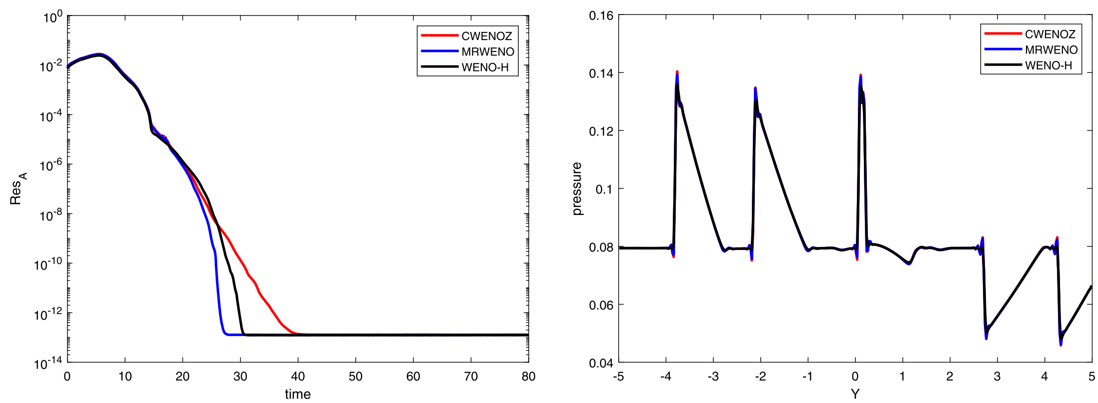

Fig. 4.22. Numerical results of Example 4.9 with mesh size 400 × 400. Left: the history of average residue of different schemes; right: 1D cut along $x = 8 - \frac{\Delta x}{2}$ for different schemes.

in Fig. 4.23. It seems that the contours of the WENO-H scheme look sharp. It is verified by the pressure distributions along the line $x = 8 - \frac{\Delta x}{2}$ in Fig. 4.22. Similarly, the hybrid one shows a better transition near discontinuities.

Example 4.10. A supersonic flow past a long plate with angle $\theta = 10°$. The initial condition is given by $(\rho, u, v, P) = (1, \cos(\theta), \sin(\theta), \frac{1}{9\gamma})$, where $\gamma = 1.4$. We compute this problem in a rectangular $[0, 7] \times [-5, 5]$. The long plate is located at $[2, 7] \times \{0\}$, and the slip boundary condition is imposed on it. The inflow boundary condition is applied along the left and bottom boundaries, while the outflow boundary condition is applied along the right and top boundaries. We present the results when the numerical solutions have reached their steady states. The time history of the average residue

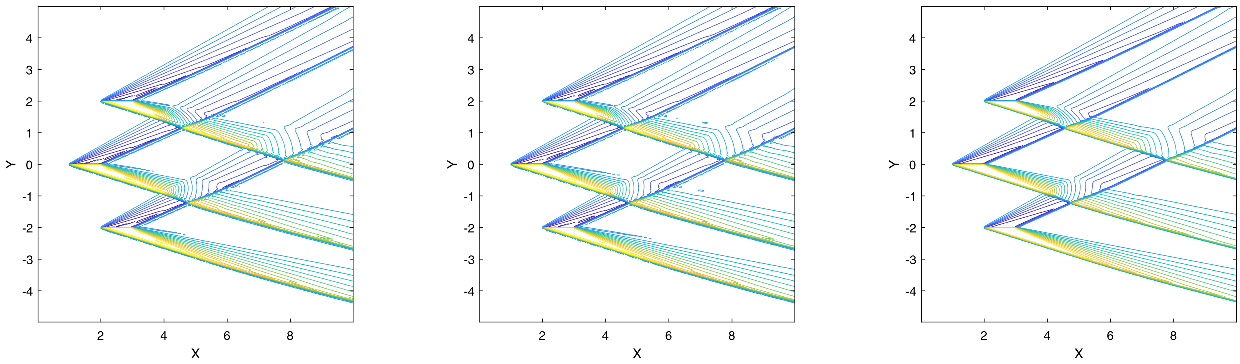

Fig. 4.23. Pressure contours of different schemes for Example 4.9 with mesh size 400 × 400. 30 equally spaced contour lines from 0.02 to 0.23. Left: result of the CWENOZ scheme; center: result of the MRWENO scheme; right: result of the WENO-H scheme.

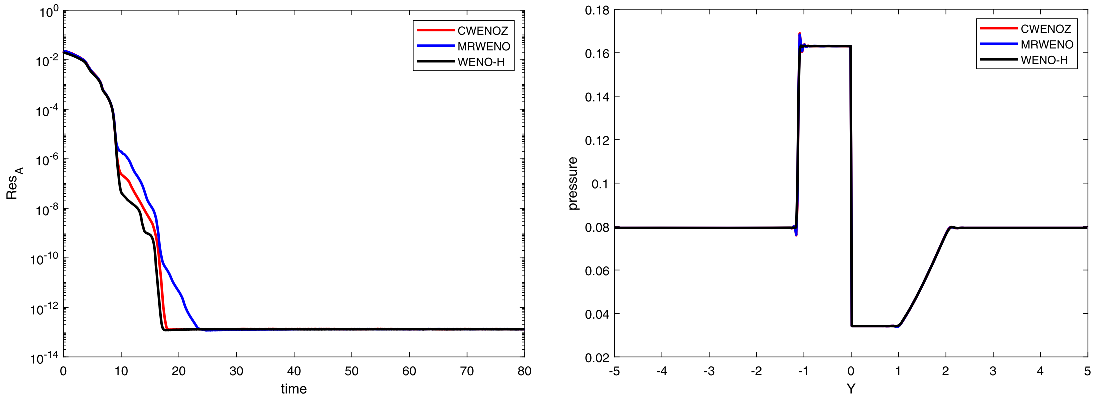

Fig. 4.24. Numerical results of Example 4.10 with mesh size 280 × 400. Left: the history of average residue of different schemes; right: 1D cut along $x = 5.6 - \frac{\Delta x}{2}$ for different schemes.

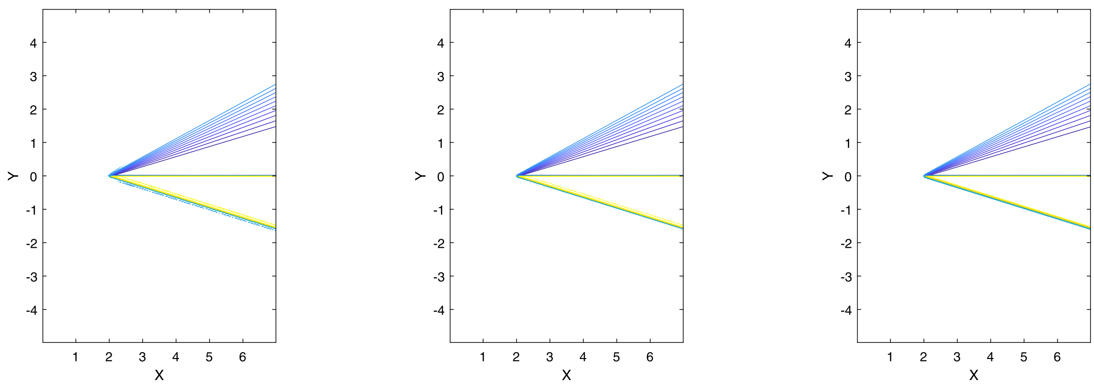

Fig. 4.25. Pressure contours of different schemes for Example 4.10 with mesh size 280 × 400. 30 equally spaced contour lines from 0.031 to 0.161. Left: result of the CWENOZ scheme; center: result of the MRWENO scheme; right: result of the WENO-H scheme.

is presented in Fig. 4.24, which shows that the average residue of all schemes can settle down to a value around 10^{-13}. The pressure contours of the numerical solutions are shown in Fig. 4.25, from which it is also found that the contours of the WENO-H scheme look sharp and clear. The pressure distributions along the line $x = 5.6 - \frac{\Delta x}{2}$ are also shown in Fig. 4.24, which verifies that the hybrid one suppresses numerical oscillation better than the CWENOZ and MRWENO schemes.

Example 4.11. A supersonic flow past three long plates with angle $\theta = 10°$. The initial condition is given by $(\rho, u, v, P) = (1, \cos(\theta), \sin(\theta), \frac{1}{9\gamma})$, where $\gamma = 1.4$. We compute this problem in a rectangular $[0, 5] \times [-5, 5]$. The first long plate is located at $[2, 5] \times \{-2\}$, the second long plate is located at $[2, 5] \times \{0\}$, and the third long plate is located at $[2, 5] \times \{2\}$. The slip boundary condition is imposed on these plates. The inflow boundary condition is applied along the left and

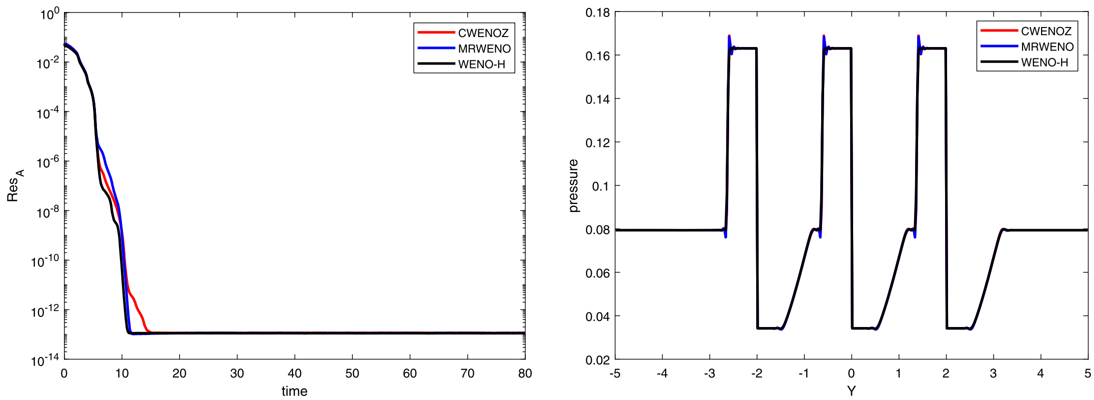

Fig. 4.26. Numerical results of Example 4.11 with mesh size 200 × 400. Left: the history of average residue of different schemes; right: 1D cut along $x = 4 - \frac{\Delta x}{2}$ for different schemes.

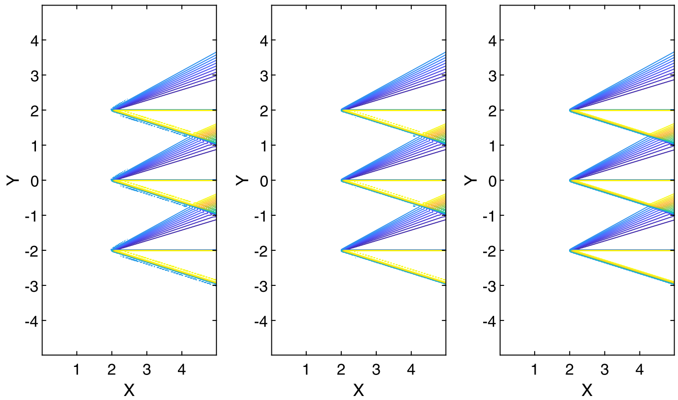

Fig. 4.27. Pressure contours of different schemes for Example 4.11 with mesh size 200 × 400. 30 equally spaced contour lines from 0.031 to 0.161. Left: result of the CWENOZ scheme; center: result of the MRWENO scheme; right: result of the WENO-H scheme.

bottom boundaries, while the outflow boundary condition is applied along the right and top boundaries. We present the results when the numerical solutions have reached their steady states. The time history of the average residue is presented in Fig. 4.26. The average residue of all schemes can settle down to a value around 10^{-13}. The pressure contours of the numerical solutions are shown in Fig. 4.27. It looks that the contours of the WENO-H scheme are sharp and clear. The pressure distributions along the line $x = 4 - \frac{\Delta x}{2}$ in Fig. 4.26 verify that the hybrid one achieves the essentially non-oscillation property better. At the same time, some oscillations appear in the results computed by the CWENOZ and MRWENO schemes.

Example 4.12. A supersonic flow past a square column with angle $\theta = 0^\circ$. The initial condition is given by $(\rho, u, v, P) = (1, 1, 0, \frac{1}{16\gamma})$, where $\gamma = 1.4$. We compute this problem in a rectangular $[-5, 5] \times [-9, 9]$. The square column is located at $[1, 5] \times [-0.5, 0.5]$, imposing the slip boundary condition. The inflow and outflow boundary conditions are applied along the outer boundaries. We present the results when the numerical solutions have reached their steady states. First, we compute this problem with mesh size 60 × 108. The time history of the average residue is presented in Fig. 4.28. We can see that the average residue of all schemes can settle down to a value around 10^{-14}. The pressure contours of the numerical solutions are shown in Fig. 4.29, and the pressure distributions along the line $x = 9 - \frac{\Delta x}{2}$ are also shown in Fig. 4.28. It can be seen that all schemes can solve this problem well.

Next, we compute this problem with mesh size 120 × 216. The time history of the average residue is presented in Fig. 4.30. It can be found that the average residue of all schemes can settle down to a value around $10^{-13.5}$ except the CWENOZ scheme. Notice that the CWENOZ(1.1) scheme can solve this issue. The pressure contours of the numerical solutions are shown in Fig. 4.31. The pressure distributions along the line $x = 9 - \frac{\Delta x}{2}$ are also shown in Fig. 4.30. Once again, the hybrid one suppresses numerical oscillations better than other WENO schemes based on the performances near $y = \pm 4$, and the hybrid one presents sharper transition near discontinuities based on the performances near $y = \pm 0.5$.

Example 4.13. A supersonic flow past two square columns with angle $\theta = 0^\circ$. The initial condition is given by $(\rho, u, v, P) = (1, 1, 0, \frac{1}{16\gamma})$, where $\gamma = 1.4$. We compute this problem in a rectangular $[-5, 5] \times [-9, 9]$. The first square column is located at $[1, 5] \times [-4.5, -3.5]$, and the second square column is located at $[1, 5] \times [3.5, 4.5]$. We impose the slip boundary condition

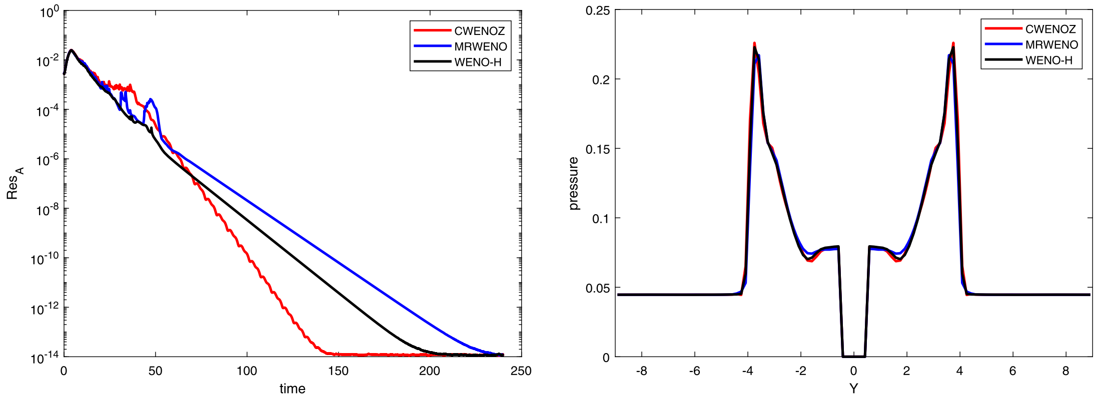

Fig. 4.28. Numerical results of Example 4.12 with mesh size 60×108. Left: the history of average residue of different schemes; right: 1D cut along $x = 9 - \frac{\Delta x}{2}$ for different schemes.

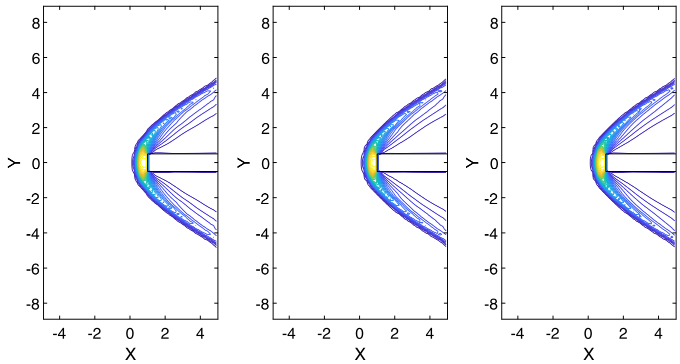

Fig. 4.29. Pressure contours of different schemes for Example 4.12 with mesh size 60×108. 30 equally spaced contour lines from 0.05 to 0.87. Left: result of the CWENOZ scheme; center: result of the MRWENO scheme; right: result of the WENO-H scheme.

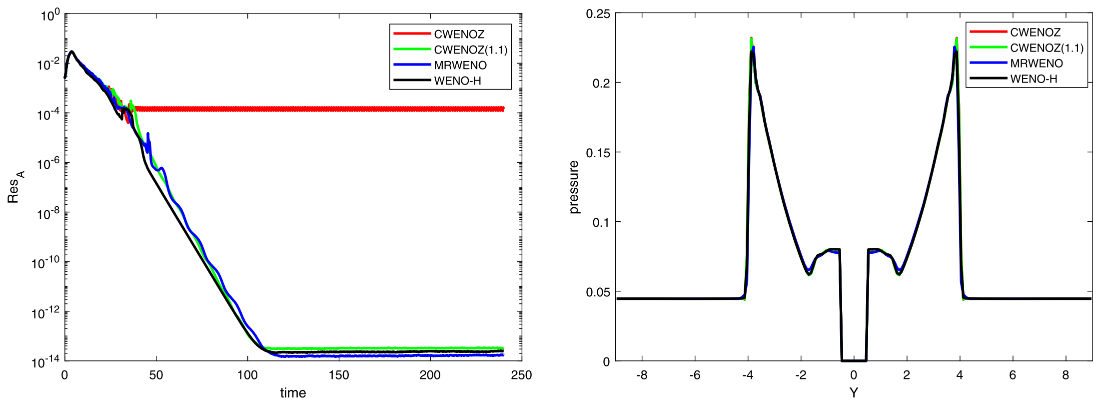

Fig. 4.30. Numerical results of Example 4.12 with mesh size 120×216. Left: the history of average residue of different schemes; right: 1D cut along $x = 9 - \frac{\Delta x}{2}$ for different schemes.

on these columns. The inflow and outflow boundary conditions are applied along the outer boundaries. We present the results when the numerical solutions have reached their steady states. First, we compute this problem with mesh size 80×144. The time history of the average residue is presented in Fig. 4.32. We can see that the average residue of all schemes can settle down to a value around 10^{-14}. The pressure contours of the numerical solutions are shown in Fig. 4.33, and the pressure distributions along the line $x = 6 - \frac{\Delta x}{2}$ are shown in Fig. 4.32. It can be found that all schemes could solve this problem well.

Second, we compute this problem with mesh size 160×288. The time history of the average residue is presented in Fig. 4.34. In this case, we see that the average residue of all schemes can settle down to a value around $10^{-13.5}$ except

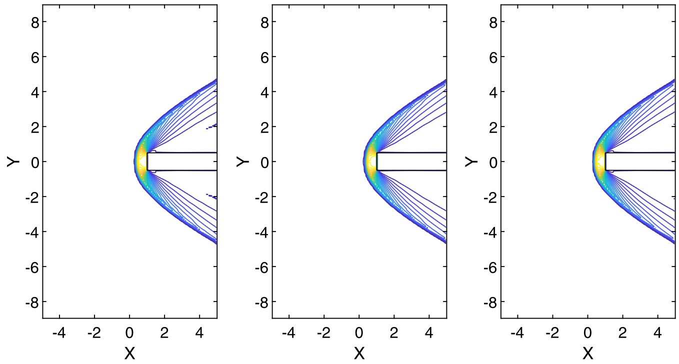

Fig. 4.31. Pressure contours of different schemes for Example 4.12 with mesh size 120×216. 30 equally spaced contour lines from 0.05 to 0.87. Left: result of the CWENOZ scheme; center: result of the MRWENO scheme; right: result of the WENO-H scheme.

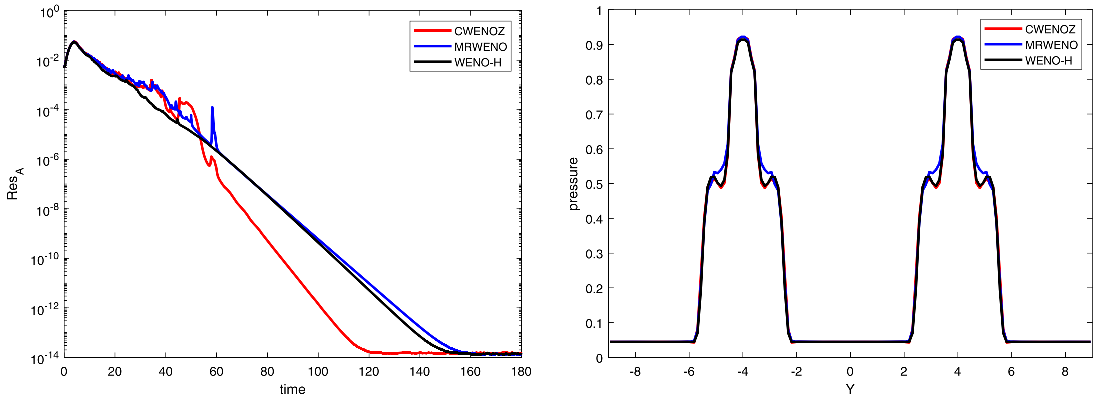

Fig. 4.32. Numerical results of Example 4.13 with mesh size 80×144. Left: the history of average residue of different schemes; right: 1D cut along $x = 6 - \frac{\Delta x}{2}$ for different schemes.

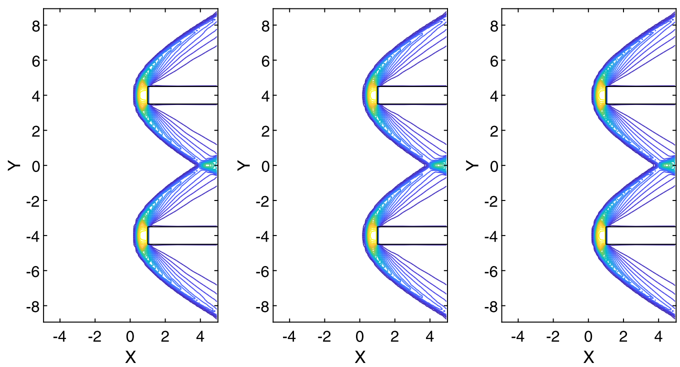

Fig. 4.33. Pressure contours of different schemes for Example 4.13 with mesh size 80×144. 30 equally spaced contour lines from 0.05 to 0.87. Left: result of the CWENOZ scheme; center: result of the MRWENO scheme; right: result of the WENO-H scheme.

for the CWENOZ scheme, but CWENOZ(1.1) scheme works. The pressure contours of the numerical solutions are shown in Fig. 4.35. The pressure distributions along the line $x = 6 - \frac{\Delta x}{2}$ are also shown in Fig. 4.34, from which it can be found that the result of the hybrid one is slightly less oscillatory.

Example 4.14. Three-dimensional Euler quations with source terms. The source term $(0.6\cos(x+y+z), 0.8\cos(x+y+z), 0.8\cos(x+y+z), 0.8\cos(x+y+z), 3\cos(x+y+z))^T$ is added to the right hand side of equations (1.1), and the exact steady-state solutions are $(\rho, u, v, w, P)^T = (1 + 0.2\sin(x+y+z), 1, 1, 1, 1 + 0.2\sin(x+y+z))^T$. We compute this problem in a cube domain $[0, 2\pi]^3$ with the CFL number 0.6, and the boundary conditions of all the directions are imposed by the exact solutions. The accuracy test results are listed in Table 4.3, and the final computational time is $T = 40$. The results of the CWENOZ and MRWENO schemes are omitted for simplicity since they are similar to the result of the WENO-H scheme.

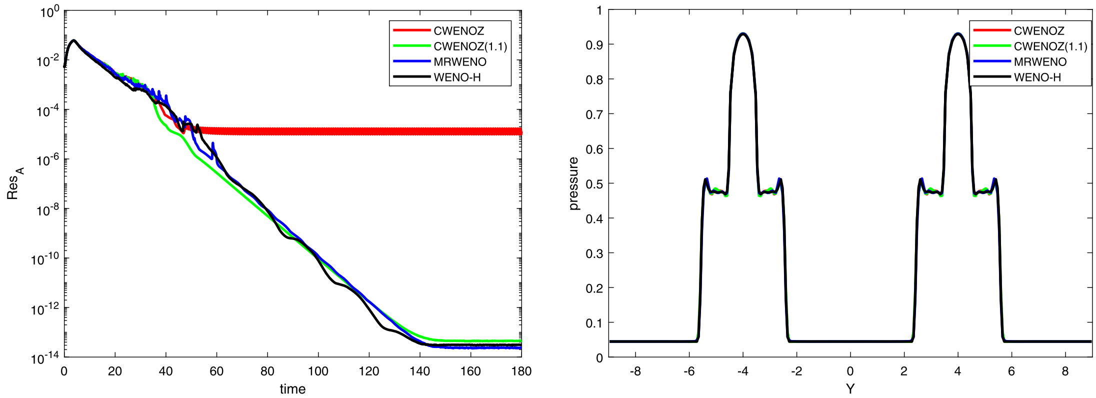

Fig. 4.34. Numerical results of Example 4.13 with mesh size 160×288. Left: the history of average residue of different schemes; right: 1D cut along $x = 6 - \frac{\Delta x}{2}$ for different schemes.

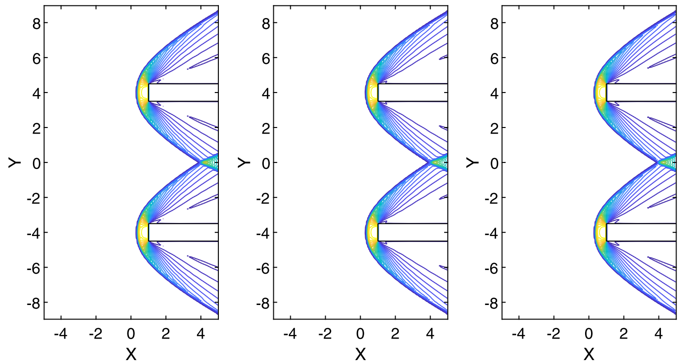

Fig. 4.35. Pressure contours of different schemes for Example 4.13 with mesh size 160×288. 30 equally spaced contour lines from 0.05 to 0.87. Left: result of the CWENOZ scheme; center: result of the MRWENO scheme; right: result of the WENO-H scheme.

Table 4.3
L^1 and L^∞ errors of different schemes for Example 4.14. Steady state.

$N_x \times N_y \times N_z$	UW5				WENO-H			
	L^1 error	order	L^∞ error	order	L^1 error	order	L^∞ error	order
$20 \times 20 \times 20$	3.90E-03	––	5.76E-05	––	3.90E-03	––	5.76E-05	––
$30 \times 30 \times 30$	5.00E-04	5.07	7.35E-06	5.08	5.00E-04	5.07	7.35E-06	5.08
$40 \times 40 \times 40$	1.17E-04	5.04	1.73E-06	5.03	1.17E-04	5.04	1.73E-06	5.03
$50 \times 50 \times 50$	3.82E-05	5.03	5.65E-07	5.01	3.82E-05	5.03	5.65E-07	5.01
$60 \times 60 \times 60$	1.53E-05	5.01	2.27E-07	5.01	1.53E-05	5.01	2.27E-07	5.01
$70 \times 70 \times 70$	7.06E-06	5.01	1.05E-07	5.02	7.06E-06	5.01	1.05E-07	5.02

We can see that the WENO-H scheme achieves the designed fifth-order accuracy. We show the time history of the average residue in Fig. 4.36. It shows that the average residue of the WENO-H scheme can settle down to tiny values close to machine zero.

Example 4.15. A 3D Mach 3 flow past a plate. The initial condition is given by $(\rho, u, v, w, P) = (1, \frac{\sqrt{3}}{3}, \frac{\sqrt{3}}{3}, \frac{\sqrt{3}}{3}, \frac{1}{9\gamma})$. We compute this problem in a cube domain $[-5, 5]^3$ with the CFL number 0.6. The plate is located at $[0, 2] \times \{0\} \times [-1, 1]$, and the slip boundary condition is imposed on it. The inflow and outflow boundary conditions are applied along the outer boundaries. We compute this problem with mesh size $100 \times 100 \times 100$. The CWENOZ scheme fails to solve this problem due to negative pressure. However, the modified CWENOZ scheme with linear weights $(d_1, d_2, d_3) = (0.8, 0.1, 0.1)$ can solve this problem. The time history of the average residue is presented in Fig. 4.37, from which we can see that the numerical solutions computed by all schemes can converge to the steady state except the MRWENO scheme. The pressure contours of the numerical solution computed by the WENO-H scheme are shown in Fig. 4.38. The results computed by the modified CWENOZ and MRWENO schemes are omitted for simplicity since they are similar to that of the WENO-H scheme.

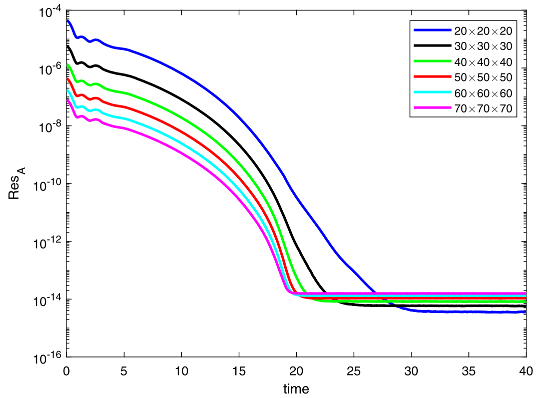

Fig. 4.36. Average residue history of the WENO-H scheme for Example 4.14.

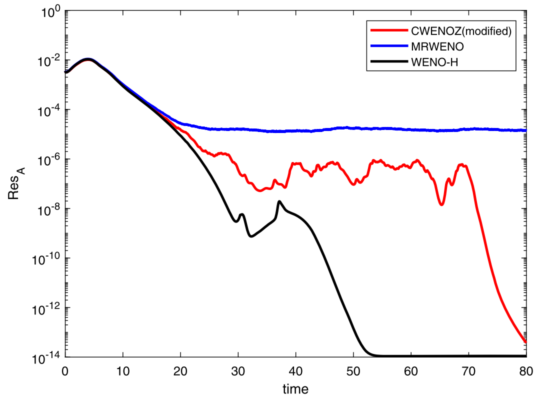

Fig. 4.37. Average residue history of different schemes for Example 4.15.

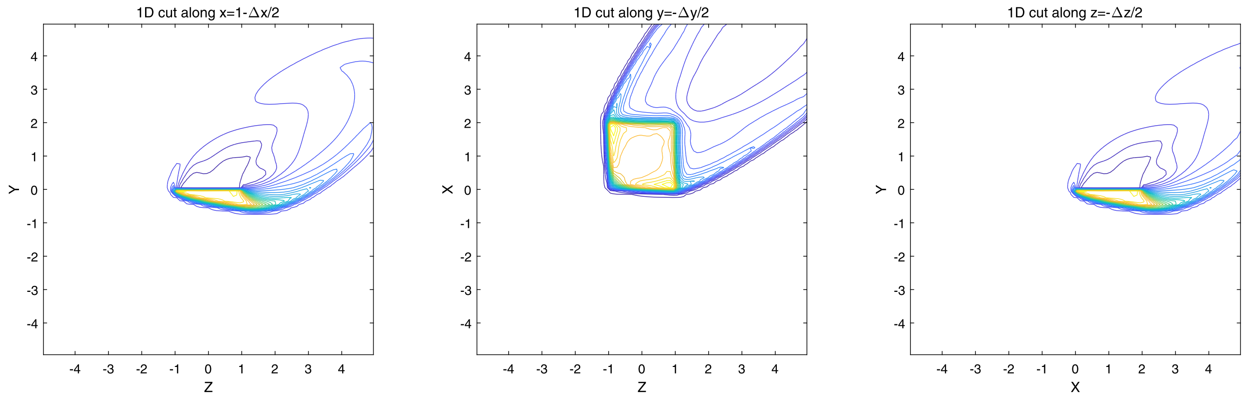

Fig. 4.38. Pressure contours of the WENO-H scheme for Example 4.15 with mesh size $100 \times 100 \times 100$. 30 equally spaced contour lines from 0.0 to 0.6.

5. Conclusion

In this paper, we proposed a hybrid approach to the fifth-order WENO scheme for the steady-state problems of Euler equations. Inspired by the work in [52], the reconstruction stencil was identified as smooth, non-smooth, and transition regions by adopting a simple and effective smoothness detector. The linear and blending reconstructions applied on the smooth and non-smooth regions aimed to increase the spectral resolution, verified by the approximate spectral analysis and numerous numerical examples. Meanwhile, the blending and transition reconstructions adopted on the non-smooth and transition regions aimed to overcome the difficulty of residue convergence caused by strong discontinuities. In all the benchmarks of our numerical tests, the average residue of the hybrid scheme could settle down to the round-off error level successfully. Besides, the hybrid scheme presented the numerical solutions with better robustness and essentially non-oscillatory property than the newly proposed schemes [66,69] used to solve steady-state problems and maintained the sharp resolution near shocks. For strong shock waves, this hybrid approach possesses a good potential to be adapted for other high order reconstructions and numerical schemes.

CRediT authorship contribution statement

Yifei Wan: Conceptualization, Methodology, Software, Writing – original draft, Writing – review & editing. **Yinhua Xia:** Conceptualization, Methodology, Writing – original draft, Writing – review & editing.

Declaration of competing interest

The authors declare that they have no known competing financial interests or personal relationships that could have appeared to influence the work reported in this paper.

References

[1] F. Acker, R.B. de, R. Borges, B. Costa, An improved WENO-Z scheme, J. Comput. Phys. 313 (2016) 726–753.
[2] N.A. Adams, K. Shariff, A high-resolution hybrid compact-ENO scheme for shock-turbulence interaction problems, J. Comput. Phys. 127 (1) (1996) 27–51.
[3] A.A. Bhise, R. Samala, An efficient hybrid WENO scheme with a problem independent discontinuity locator, Int. J. Numer. Methods Fluids 91 (1) (2019) 1–28.
[4] R. Borges, M. Carmona, B. Costa, W.-S. Don, An improved weighted essentially non-oscillatory scheme for hyperbolic conservation laws, J. Comput. Phys. 227 (6) (2008) 3191–3211.
[5] G. Capdeville, A central WENO scheme for solving hyperbolic conservation laws on non-uniform meshes, J. Comput. Phys. 227 (5) (2008) 2977–3014.
[6] S. Chen, Fixed-point fast sweeping WENO methods for steady state solution of scalar hyperbolic conservation laws, Int. J. Numer. Anal. Model. 11 (1) (2014) 117–130.
[7] W. Chen, C.-S. Chou, C.-Y. Kao, Lax–Friedrichs fast sweeping methods for steady state problems for hyperbolic conservation laws, J. Comput. Phys. 234 (2013) 452–471.
[8] W. Chen, C.-S. Chou, C.-Y. Kao, Lax–Friedrichs multigrid fast sweeping methods for steady state problems for hyperbolic conservation laws, J. Sci. Comput. 64 (3) (2015) 591–618.
[9] B. Cockburn, C.-W. Shu TVB, Runge-Kutta local projection discontinuous Galerkin finite element method for conservation laws. ii. General framework, Math. Comput. 52 (186) (1989) 411–435.
[10] B. Costa, W.-S. Don, Multi-domain hybrid spectral-WENO methods for hyperbolic conservation laws, J. Comput. Phys. 224 (2) (2007) 970–991.
[11] I. Cravero, G. Puppo, M. Semplice, G. Visconti, CWENO: uniformly accurate reconstructions for balance laws, Math. Comput. 87 (312) (2018) 1689–1719.
[12] I. Cravero, M. Semplice, G. Visconti, Optimal definition of the nonlinear weights in multidimensional central WENOZ reconstructions, SIAM J. Numer. Anal. 57 (5) (2019) 2328–2358.
[13] W.-S. Don, Z. Gao, P. Li, X. Wen, Hybrid compact-WENO finite difference scheme with conjugate Fourier shock detection algorithm for hyperbolic conservation laws, SIAM J. Sci. Comput. 38 (2) (2016) A691–A711.
[14] B. Engquist, B.D. Froese, Y.-H.R. Tsai, Fast sweeping methods for hyperbolic systems of conservation laws at steady state, J. Comput. Phys. 255 (2013) 316–338.
[15] B. Engquist, B.D. Froese, Y.-H.R. Tsai, Fast sweeping methods for hyperbolic systems of conservation laws at steady state ii, J. Comput. Phys. 286 (2015) 70–86.
[16] J. Fernández-Fidalgo, X. Nogueira, L. Ramírez, I. Colominas, An a posteriori, efficient, high-spectral resolution hybrid finite-difference method for compressible flows, Comput. Methods Appl. Mech. Eng. 335 (2018) 91–127.
[17] L. Fu, A hybrid method with TENO based discontinuity indicator for hyperbolic conservation laws, Commun. Comput. Phys. 26 (4) (2019) 973–1007.
[18] L. Fu, X.Y. Hu, N.A. Adams, A family of high-order targeted ENO schemes for compressible-fluid simulations, J. Comput. Phys. 305 (2016) 333–359.
[19] L. Fu, X.Y. Hu, N.A. Adams, Targeted ENO schemes with tailored resolution property for hyperbolic conservation laws, J. Comput. Phys. 349 (2017) 97–121.
[20] S. Gottlieb, C.-W. Shu, E. Tadmor, Strong stability-preserving high-order time discretization methods, SIAM Rev. 43 (2001) 89–112.
[21] W. Hao, J.D. Hauenstein, C.-W. Shu, A.J. Sommese, Z. Xu, Y.-T. Zhang, A homotopy method based on WENO schemes for solving steady state problems of hyperbolic conservation laws, J. Comput. Phys. 250 (2013) 332–346.
[22] A. Harten, Adaptive multiresolution schemes for shock computations, J. Comput. Phys. 115 (2) (1994) 319–338.
[23] A. Harten, B. Engquist, S. Osher, S.R. Chakravarthy, Uniformly high order accurate essentially non-oscillatory schemes, iii, J. Comput. Phys. 131 (1) (1987) 3–47.
[24] A.K. Henrick, T.D. Aslam, J.M. Powers, Mapped weighted essentially non-oscillatory schemes: achieving optimal order near critical points, J. Comput. Phys. 207 (2) (2005) 542–567.
[25] G. Hu, X. Meng, N. Yi, Adjoint-based an adaptive finite volume method for steady Euler equations with non-oscillatory k-exact reconstruction, Comput. Fluids 139 (2016) 174–183.
[26] G. Hu, N. Yi, An adaptive finite volume solver for steady Euler equations with non-oscillatory k-exact reconstruction, J. Comput. Phys. 312 (2016) 235–251.
[27] X. Ji, F. Zhao, W. Shyy, K. Xu, A family of high-order gas-kinetic schemes and its comparison with Riemann solver based high-order methods, J. Comput. Phys. 356 (2018) 150–173.
[28] G.-S. Jiang, C.-W. Shu, Efficient implementation of weighted ENO schemes, J. Comput. Phys. 126 (1) (1996) 202–228.
[29] L. Krivodonova, J. Xin, J.-F. Remacle, N. Chevaugeon, J.E. Flaherty, Shock detection and limiting with discontinuous Galerkin methods for hyperbolic conservation laws, Appl. Numer. Math. 48 (3–4) (2004) 323–338.
[30] D. Levy, G. Puppo, G. Russo, Central WENO schemes for hyperbolic systems of conservation laws, Math. Model. Numer. Anal. 33 (3) (1999) 547–571.
[31] D. Levy, G. Puppo, G. Russo, Compact central WENO schemes for multidimensional conservation laws, SIAM J. Sci. Comput. 22 (2) (2000) 656–672.
[32] C. Li, D. Sun, Q. Guo, P. Liu, H. Zhang, A new hybrid WENO scheme on a four-point stencil for Euler equations, J. Sci. Comput. 87 (1) (2021) 1–37.
[33] G. Li, C. Lu, J. Qiu, Hybrid well-balanced WENO schemes with different indicators for shallow water equations, J. Sci. Comput. 51 (2012) 527–559.
[34] G. Li, J. Qiu, Hybrid weighted essentially non-oscillatory schemes with different indicators, J. Comput. Phys. 229 (2010) 8105–8129.
[35] G. Li, J. Qiu, Hybrid WENO schemes with different indicators on curvilinear grid, Adv. Comput. Math. 40 (2014) 747–772.

[36] L. Li, J. Zhu, Y.-T. Zhang, Absolutely convergent fixed-point fast sweeping WENO methods for steady state of hyperbolic conservation laws, J. Comput. Phys. 443 (2021) 110516.
[37] S. Liu, Y. Shen, F. Zeng, M. Yu, A new weighting method for improving the WENO-Z scheme, Int. J. Numer. Methods Fluids 87 (6) (2018) 271–291.
[38] X.-D. Liu, S. Osher, T. Chan, Weighted essentially non-oscillatory schemes, J. Comput. Phys. 115 (1) (1994) 200–212.
[39] X. Luo, S.-P. Wu, Improvement of the WENO-Z+ scheme, Comput. Fluids 218 (2021) 104855.
[40] X. Meng, G. Hu, A NURBS-enhanced finite volume solver for steady Euler equations, J. Comput. Phys. 359 (2018) 77–92.
[41] C.S. Peskin, The immersed boundary method, Acta Numer. 11 (2002) 479–517.
[42] S. Pirozzoli, Conservative hybrid compact-WENO schemes for shock-turbulence interaction, J. Comput. Phys. 178 (1) (2002) 81–117.
[43] S. Pirozzoli, On the spectral properties of shock-capturing schemes, J. Comput. Phys. 219 (2) (2006) 489–497.
[44] J. Qiu, C.-W. Shu, A comparison of troubled-cell indicators for Runge-Kutta discontinuous Galerkin methods using weighted essentially nonoscillatory limiters, SIAM J. Sci. Comput. 27 (3) (2005) 995–1013.
[45] S. Rathan, G.N. Raju, A modified fifth-order WENO scheme for hyperbolic conservation laws, Comput. Math. Appl. 75 (5) (2018) 1531–1549.
[46] Y.-X. Ren, M. Liu, H. Zhang, A characteristic-wise hybrid compact-WENO scheme for solving hyperbolic conservation laws, J. Comput. Phys. 192 (2) (2003) 365–386.
[47] S. Serna, A. Marquina, Power ENO methods: a fifth-order accurate weighted power ENO method, J. Comput. Phys. 194 (2) (2004) 632–658.
[48] C.-W. Shu, High order weighted essentially nonoscillatory schemes for convection dominated problems, SIAM Rev. 51 (1) (2009) 82–126.
[49] C.-W. Shu, S. Osher, Efficient implementation of essentially non-oscillatory shock-capturing schemes, II, J. Comput. Phys. 83 (1) (1989) 32–78.
[50] Z. Sun, S. Wang, L.-B. Chang, Y. Xing, D. Xiu, Convolution neural network shock detector for numerical solution of conservation laws, Commun. Comput. Phys. 28 (5) (2020) 2075–2108.
[51] A. Suresh, H.T. Huynh, Accurate monotonicity-preserving schemes with Runge-Kutta time stepping, J. Comput. Phys. 136 (1) (1997) 83–99.
[52] Y. Wan, Y. Xia, A new hybrid WENO scheme with the high-frequency region for hyperbolic conservation laws, Commun. Appl. Math. Comput. (2021), https://doi.org/10.1007/s42967-021-00153-2.
[53] B.S. Wang, W.-S. Don, Z. Gao, Y.H. Wang, X. Wen, Hybrid compact-WENO finite difference scheme with radial basis function based shock detection method for hyperbolic conservation laws, SIAM J. Sci. Comput. 40 (6) (2018) A3699–A3714.
[54] X. Wen, W.-S. Don, Z. Gao, J.S. Hesthaven, An edge detector based on artificial neural network with application to hybrid compact-WENO finite difference scheme, J. Sci. Comput. 83 (2020) 49.
[55] P. Woodward, P. Colella, The numerical simulation of two-dimensional fluid flow with strong shocks, J. Comput. Phys. 54 (1) (1984) 115–173.
[56] L. Wu, Y.-T. Zhang, S. Zhang, C.-W. Shu, High order fixed-point sweeping WENO methods for steady state of hyperbolic conservation laws and its convergence study, Commun. Comput. Phys. 20 (4) (2016) 835–869.
[57] W. Xu, W. Wu, An improved third-order weighted essentially non-oscillatory scheme achieving optimal order near critical points, Comput. Fluids 162 (2018) 113–125.
[58] W. Xu, W. Wu, An improved third-order WENO-Z scheme, J. Sci. Comput. 75 (3) (2018) 1808–1841.
[59] S. Zhang, S. Jiang, C.-W. Shu, Improvement of convergence to steady state solutions of Euler equations with the WENO schemes, J. Sci. Comput. 47 (2) (2011) 216–238.
[60] S. Zhang, C.-W. Shu, A new smoothness indicator for the WENO schemes and its effect on the convergence to steady state solutions, J. Sci. Comput. 31 (1) (2007) 273–305.
[61] S. Zhang, J. Zhu, C.-W. Shu, A brief review on the convergence to steady state solutions of Euler equations with high-order WENO schemes, Adv. Aerodyn. 1 (1) (2019) 1–25.
[62] Z. Zhao, Y. Chen, J. Qiu, A hybrid Hermite WENO scheme for hyperbolic conservation laws, J. Comput. Phys. 405 (2020) 109175.
[63] Z. Zhao, J. Zhu, Y. Chen, J. Qiu, A new hybrid WENO scheme for hyperbolic conservation laws, Comput. Fluids 179 (2019) 422–436.
[64] H. Zhu, J. Qiu, Adaptive Runge-Kutta discontinuous Galerkin methods using different indicators: one-dimensional case, J. Comput. Phys. 228 (18) (2009) 6957–6976.
[65] J. Zhu, J. Qiu, A new fifth order finite difference WENO scheme for solving hyperbolic conservation laws, J. Comput. Phys. 318 (2016) 110–121.
[66] J. Zhu, C.-W. Shu, Numerical study on the convergence to steady state solutions of a new class of high order WENO schemes, J. Comput. Phys. 349 (2017) 80–96.
[67] J. Zhu, C.-W. Shu, A new type of multi-resolution WENO schemes with increasingly higher order of accuracy, J. Comput. Phys. 375 (2018) 659–683.
[68] J. Zhu, C.-W. Shu, Numerical study on the convergence to steady-state solutions of a new class of finite volume WENO schemes: triangular meshes, Shock Waves 29 (1) (2019) 3–25.
[69] J. Zhu, C.-W. Shu, Convergence to steady-state solutions of the new type of high-order multi-resolution WENO schemes: a numerical study, Commun. Appl. Math. Comput. 2 (3) (2020) 429–460.
[70] J. Zhu, C.-W. Shu, J. Qiu, High-order Runge-Kutta discontinuous Galerkin methods with multi-resolution WENO limiters for solving steady-state problems, Appl. Numer. Math. 165 (2021) 482–499.